phdtransferreportECS - AFM+Crest

UNIVERSITY OF SOUTHAMPTON

FACULTY OF ENGINEERING AND THE ENVIRONMENT

Aerodynamics and Flight Mechanics

Investigation of Single and Tandem Flapping Hydrofoils

by

Nikolaos S. Lagopoulos
ORCID ID: 0000-0001-5431-9146

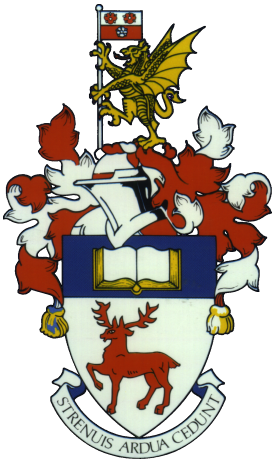

Thesis for the degree of Doctor of Philosophy

February 2021

UNIVERSITY OF SOUTHAMPTON

ABSTRACT

FACULTY OF ENGINEERING AND THE ENVIRONMENT
Aerodynamics and Flight Mechanics

Doctor of Philosophy

INVESTIGATION OF SINGLE AND TANDEM FLAPPING HYDROFOILS

by Nikolaos S. Lagopoulos
ORCID ID: 0000-0001-5431-9146

Marine vertebrates are well known to generate thrust via the oscillatory motion of blade-like body parts (e.g flippers, tails, fins, etc.). These configurations, often depicted as *flapping floils* in a two dimensional domain, demonstrate impressive manoeuvrability (Read et al., 2003) without the control imprecision exhibited by contemporary man-made designs (Kato, 1998). In this project, we investigate a bio-inspired approach of underwater propulsion, using single and tandem configurations of periodically flapping hydrofoils. Our main goal is to develop a fundamental understanding of the complex hydrodynamic interactions among shedding vortices that lead to the thrust generation of these systems. To this end we numerically analyse the wake development of the 2D single flapping foil under the influence of varying harmonic and non-harmonic kinematics and profile thickness. We find that the cycle-averaged trajectory $\mathcal{T}$ of the foil is sufficient to characterise the drag to thrust wake transition regardless of the chosen periodic motion but only for thicknesses $\sim 10\% - 16\%$ of the chord length due to limitations of the two dimensional field assumption. Moreover, we investigate the 2D interaction of deflected wakes in a tandem configuration. Our computational results reveal that a properly tuned back foil is capable of cancelling the wake deflection and mean side force of the front foil, with a subsequent increase in the overall thrust of the system. Finally, we expand the results of a previous study (Muscutt et al., 2017b) by analysing the effect of aspect ratio (AR) on a paleobiomimetic system of tandem foils. In a similar fashion to steady wing configurations, flume tank experiments suggest an improvement in terms of efficiency and thrust coefficient with increasing AR accompanied by a noticeable penalty in manoeuvrability. Yet vortex breaking along the span of highly elongated flippers mitigates these benefits as more energy is diverted towards side force.

Contents

List of Figures

List of Tables

Nomenclature

Acronyms

AR	Aspect Ratio
$BDIM$	Boundary Data Immersion Method
BvK	*Benard von Kármán*
CFD	Computational Fluid Dynamics
LE	Leading Edge
LEV	Leading Edge Vortex
MAV	Micro Air Vehicle
TE	Trailing Edge
TEV	Trailing Edge Vortex
AFM	Aerodynamics and Flight Mechanics
FSI	Fluid - Structure Interaction

Greek Symbols

α	Instantaneous effective angle of attack
Δ	Subtraction
ϵ	Infinitesimal quantity
η	Propulsive efficiency
γ	Vorticity magnitude
λ	Taper ratio
μ	Dynamic viscosity
ν	Kinematic viscosity

ω Vorticity magnitude

ϕ Inter foil phase angle

ψ Phase difference between heave and pitch

Σ Summation

θ Instantaneous pitching angle

Roman Symbols

$\mathcal{C}$ Chord length

$\mathcal{E}$ Uncertainty

$\mathcal{F}$ Data aquisition frequency

$\mathcal{P}$ Pivot point

$\mathcal{S}$ Inter foil spacing

$\mathcal{T}$ Cycle and chordwise averaged trajectory

B Calibration constant

C Load coefficient

D Foil thickness

F Force

f Flapping frequency

G Wing area

h Instantaneous lateral position of foil

L Length scale

M Moment

m Mass

n Grid resolution

p Proportionality constant

Re Reynolds number

St Strouhal number

Tr Cycle averaged trajectory

U	Velocity
u	Streamwise velocity component
v	Crossflow velocity component
W	Wing span

Superscripts

$*$	Relative quantity
$\dot{}$	Time derivative
$\tilde{}$	Averaged quantity (small version)
$\widetilde{}$	Averaged quantity (large version)

Subscripts

0	Amplitude of a periodic function
γ	Vortex induced
∞	Freestream
$\mathcal{C}$	Chord normalised
$\mathcal{L}$	Lift (side) force in 3D
$\mathcal{S}$	Spacing normalised
$\mathcal{T}$	Averaged Trajectory normalised
b	Back foil
D	Thickness normalised
d	Related to wake deflection
f	Front foil
I	Inflow
l	Lift (side) force in 2D
M	Pitching moment in 3D
m	Pitching moment in 2D
max	Maximum quantity
P	Power in 3D

p	Power in 2D
s	Single foil
T	Thrust force in 3D
t	Thrust force in 2D
x	Stream wise direction
y	Lateral direction
z	Directed towards the viewer

Declaration of Authorship

I, Nikolaos S. Lagopoulos
ORCID ID: 0000-0001-5431-9146 , declare that the thesis entitled *Investigation of Single and Tandem Flapping Hydrofoils* and the work presented in the thesis are both my own, and have been generated by me as the result of my own original research. I confirm that:

- this work was done wholly or mainly while in candidature for a research degree at this University;
- where any part of this thesis has previously been submitted for a degree or any other qualification at this University or any other institution, this has been clearly stated;
- where I have consulted the published work of others, this is always clearly attributed;
- where I have quoted from the work of others, the source is always given. With the exception of such quotations, this thesis is entirely my own work;
- I have acknowledged all main sources of help;
- where the thesis is based on work done by myself jointly with others, I have made clear exactly what was done by others and what I have contributed myself;
- parts of this work have been published as:
  - Lagopoulos, N. S., Weymouth, G. D. Ganapathisubramani, B. (2019), Universal scaling law for drag-to-thrust wake transition in flapping foils. J. Fluid Mech. vol. 872.
  - Lagopoulos, N. S., Weymouth, G. D. Ganapathisubramani, B. (2020), Deflected wake interaction of tandem flapping foils, J. Fluid Mech. vol.903.

Signed:.....

Date:.....

Acknowledgements

The presented research is funded by the EPSRC and the Office of Naval Research on behalf of the Aerodynamics and Flight Mechanics group of the University of Southampton. At this point, I would like to express my gratitude towards my supervisors, Bharathram Ganapathisubramani and Gabriel D. Weymouth for their comprehensive feedback through out the aforementioned period. In addition, I would like to thank my dearest friend and colleague Andhini Zurman-Nasution, whose continuous technical support, was invaluable during the whole period of this research. Lastly I would like to thank Bernat Font Garcia, Luis Blay Esteban, and Tim Berk for their minor yet crucial contribution to this work.

Chapter 1

Introduction

The purpose of this study is to investigate the hydrodynamics of single and tandem flapping hydrofoils and analyse the key parameters that affect propulsive performance. More specifically, the system is examined both computationally and experimentally in terms of kinematics and geometry in two and three dimensional domains.

In this chapter, the motivations, main goals, and strategic plan of the study are presented. An overview of contemporary work in the field and a basic review of the mechanics of single and tandem flapping foils is shown in Chapter 2. To this end, we present a brief summary of the suggested hydrodynamics of *Plesiosauria* since these prehistoric marine reptiles are the only known example of underwater tandem flipper propulsion found in nature. Chapter 3 outlines our computational approach and highlights some key features of the solver used. Our main computational results, that involve published work for both single and tandem configurations, can be found in Chapters 4 and 5. Chapter 6 focuses on the main elements of the experimental setup and the calibration method used. In addition, quasi-2D and bio inspired 3D experimental test cases are discussed. Finally, the concluding remarks of the study are presented in Chapter 7.

1.1 Motivations

Today it is widely accepted that, life forms tend to adapt to their environment over time, by gradually optimizing their physiology (Darwin, 2006). Biological mechanisms are usually very efficient, they demonstrate higher performance capabilities and have a smaller impact on the environment with respect to their mechanical counterparts. Therefore, it is sensible for engineers to look for solutions to complex modern day problems into the natural world; a field known as biomimetics.

The vast majority of contemporary biomimetic marine propulsors derive their features from modern day cetaceans, marine birds (penguins) and fish. However, this project

focuses on the mimesis of prehistoric marine animals entering a completely new chapter in the field of marine biomechanics namely, paleobiomechanics (Taylor et al., 2003; Rohr and Fish, 2004). A major component of *Plesiosaurs'* propulsion is the use of tandem flippers as opposed to present day aquatic reptiles. Potential benefits of tandem configurations include a propulsive enhancement of up to 100% for the hint flipper when oscillating at certain blade to blade phases (Muscutt, 2017; Muscutt et al., 2017b).

As seen in later chapters typical applications of flapping foils expand from underwater to micro air drones (AUVs and MAVs), with recent attempts including the configurations proposed by Licht et al. (2004) and Long et al. (2006). Research implies that biomimetic drones are more maneuverable and silent that conventional ones (Weymouth et al., 2017). Therefore, since deep water research is done mainly by unmanned vessels, the impact on the local fauna can be potentially reduced.

In addition, recent studies indicate the benefits of flapping foil systems in tidal energy extraction applications. Compared to a conventional turbine, flapping foils demonstrate design simplicity, robustness, easy installation, function in shallow waters and minimal impact on wildlife (Kinsey and Dumas, 2012; Xiao and Zhu, 2014).

Flapping foils in tandem or single configurations can improve surface vessels' propulsion as well. More specifically, actively controlled oscillating hydrofoils can lead to significant thrust augmentation and stabilization of ships (Politis and Politis, 2014). Furthermore, vertical tandem flapping configurations are already implemented in sports vehicles such as kayaks and race crafts Yan et al. (2016).

In the last few decades, much research has been conducted towards single flapping flippers due to their high propulsive efficiency. It is also suggested that interaction between dorsal and caudal fins improves performance since the aft foil utilises the wake of the front (Akhtar et al., 2007). Various key parameters have been studied towards the interaction of two oscillating flippers such as spacing (Broering and Lian, 2012b), phasing, frequency, spacing and phasing (Broering and Lian, 2012a), spacing and frequency (Lian et al., 2014) and the combination of the above (Muscutt et al., 2017b).

Intrestingly although single flapping foils have been analysed for various kinematics, detailed comparison of different harmonic motions in terms of thrust and lift generation is limited (Wiens and Hosoi, 2018; Andersen et al., 2017). Moreover optimal frequency-TE amplitude ratios have not been set for tandem configurations. Here we should note that, 3D features of the flipper geometry and their impact on tandem configurations have not been studied in depth experimentally.

1.2 Objectives

This study attempts to shed light on the issues mentioned above as well as, to reveal the singular key factor that leads to wake transitions regardless of the underlying kinematics (e.g. pure heave, pure pitch, coupled etc.) and the type of transition (e.g. drag-to-thrust, straight-to-deflected-wake etc.). Furthermore, we aim to investigate the performance of tandem configurations at these transition regimes. Finally, we attempt to compare the performance of various bioinspired flippers of same and/or different swept angle and aspect ratio (AR).

To sum up, throughout the duration of this project we focus on:

- Distinguishing self-similar kinematics of single flapping foils regarding the transition regimes (drag to thrust and wake deflection) in 2D.
- Exploring the impact of tandem configurations on the wake development at transition regimes of a single foil for basic kinematics (pure pitch/heave and coupled motion).
- Evaluating the kinematic parameters (e.g. TE amplitude, frequency, type of motion) of tandem configurations in 2D towards optimal propulsive performance.
- Investigating the influence of 3D factors e.g AR, on tandem configurations of identical bioinspired flippers

Although the above topics are of great interest in many areas mentioned previously, we will focus specifically on the implementation of our findings on unmanned underwater applications. Furthermore, we will also attempt to obtain a deep understanding of the physics of this complex motion namely, describing the optimal vortex interaction between the wakes of the two foils.

1.3 Approach

Perhaps the two most important characteristics of a propulsive mechanism are the maximum thrust produced and the propulsive efficiency. Therefore, the study will focus on the optimization of the two parameters for the various cases discussed above. The initial research is conducted for 2D domains due to their simplicity compared to 3D ones. It should be noted that we also need to take into account some crucial parameters such as reliability and clarity of the findings, uncertainty and relevance of the research to real life conditions. Thus, the initial steps towards the project are related to validation of both the computational and the experimental tools. Following the suggestions of previous research (Muscutt et al., 2017a), the flapping kinematics can approximate their

biological counterparts by the superposition of harmonic pitching and harmonic heaving motions with an optimal phase difference of 90°. (Akhtar et al., 2007). Yet as mentioned pure harmonic motions and more coupled combinations will be studied thoroughly.

The CFD package (LOTUS) used has been shown to give accurate results for a great range of fluid structure interaction problems (Weymouth and Yue, 2011; Maertens and Weymouth, 2015; Weymouth, 2014; Polet et al., 2015). Within this project we optimize the solver in terms of time and grid convergence for both the single and tandem case. Time convergence is achieved when repeatable patterns of a produced variable e.g. thrust or lift, become identical in terms of waveform, amplitude and period over time. This is examined through post processing algorithms in Python, through the cycle history of the mean thrust. Furthermore, we perform grid refinement by calculating the cycle averaged thrust of the configuration for increasing mesh density. Here convergence is demonstrated as the relationship between thrust and grid density follows a power law. This means that after a certain mesh resolution the load coefficient becomes virtually independent of further refinement. It should be noted that to minimize computational effort, we chose non-uniform mesh patterns (more details in Chapter 3).

Single foil simulations are conducted for Strouhal numbers that ensure drag to thrust transition in the downstream wake. Furthermore, single and tandem configurations are simulated in Strouhal numbers that result in wake symmetry breaking within the 2 dimensional domain. Here we remind the reader that, we initially focus on the comparison among different thrust producing kinematics for the single flapping foil while later we attempt to explore the interaction of deflected wakes in a tandem configuration.

The experimental method used in this study, is the force acquisition through strain gauges connected to the oscillating body. Therefore, calibration of the system is conducted by using a force balance technique and a relevant software. All experiments are repeated multiple times to ensure repeatability and the uncertainty of the measurements is assessed accordingly (de Kat, 2016b).

The experiments are conducted for a Strouhal within the preferred range in the natural world (Taylor et al., 2003; Godoy-Diana et al., 2009; Triantafyllou et al., 1991). All test cases use the same hydrofoil profile of an Eppler 387, which was found to better approximate the cross section of a Plesiosaur flipper (Muscutt et al., 2017a; Muscutt, 2017). Quasi two dimensional studies are enabled by rectangular flippers that cover the whole span of the test section. Three dimensional designs are quite smaller ranging from 20% to 50% of the cross section span. First, the optimal effective angle of attack is found for the single quasi-2D cases. Then we proceed with the investigation of the bio-inspired configuration, by comparing the behaviour of single and tandem flipper arrangements for increasing aspect ratio.

Chapter 2

Theory

In this section, a brief summary of recent studies in single and tandem flapping motion is presented. First, basic information about the mechanics of flapping foil propulsion is shown e.g. kinematics, non-dimensional numbers etc. Later we focus on the published data regarding thrust and lift generation of the single foil and the significant thrust enhancement reported for tandem configurations. Moreover, we present the suggested swimming strategies and basic flipper geometries of *Plesiosaurs* due to their relevance towards our project. As mentioned in previous chapters this is related to the fact that plesiosaurs are the only known marine reptiles capable of utilizing both fore and back flippers to propel themselves. It is therefore safe to assume that their overall hydrodynamics are influenced by their locomotion strategy. Finally, we present the contemporary advancements in biomimetic UUV technology with a focus on flapping foil systems.

2.1 Dimensionless Quantities

Quantities with no physical dimensions are frequently used in fluid mechanics, since they enable the comparison of physically similar test cases at different scales. For the purpose of this study, we consider at least five non-dimensional quantities; the Reynolds and Strouhal numbers, the non dimensional amplitude and finally the load and efficiency coefficients. The first three enable a better interpretation of the physics behind the phenomena, while the later ones enable comparison to other means of propulsion from an engineering point of view.

The Reynolds Number (Re) is an indicator of the dominance of flow inertia over viscosity and vice versa. More specifically, high Re indicates stronger inertia and results in turbulence, whilst low Re indicates laminar highly viscous, low speed flows. Mathematically

it is expressed as

$$Re_L = \frac{LU_\infty}{\nu} \tag{2.1}$$

where U_∞ = freestream velocity, L = length scale and ν = kinematic viscosity.

As a common practice within relevant literature, the length scale chosen for this project is the chord length $\mathcal{C}$. Since we focus on underwater applications a range of high $Re_\mathcal{C}$ will be covered namely, $Re_\mathcal{C} \sim [4{\cdot}10^4 - 8{\cdot}10^5]$. However, it is useful to study lower numbers as well ($Re_\mathcal{C} < 2000$) to be consistent with literature when examining bifurcation wake phenomena (Godoy-Diana et al., 2008a)

The Strouhal Number (St_L) expresses the intensity of local instabilities around a body, with respect to the undisturbed freestream. For instance a flapping foil is a reciprocating system, generating thrust and/or lift, by vortex shedding. Here we recall the phenomenon described by *von Kármán*, where at certain Re the wake behind a stable bluff body consists of alternating vortices (Triantafyllou et al., 1986). Furthermore, special combinations of oscillating amplitude and frequency (like the ones presented later in this study) result in the $lock-in$ of the shedding and the flapping frequency (Spiker et al., 2006). Thus the Strouhal Number can be interpreted as the ratio of flapping velocity over the forward speed, or the ratio of the flapping period over the oscillating period and is defined as:

$$St_L = \frac{Lf}{U_\infty} \tag{2.2}$$

where, f = frequency of oscillation, L = characteristic length, and U_∞ = velocity of fluid.

Since we are focusing on frequencies well above the lock-in threshold, the Strouhal number can serve as a non dimensional flapping frequency. Therefore, throughout this analysis we make use of various Strouhal numbers according to the particular chosen characteristic length e.g. thickness, chord length, amplitude, trajectory of motion etc.

Another dimensionless quantity commonly used in literature, is the non-dimensional TE amplitude (A_L):

$$A_L = \frac{2A}{L} \tag{2.3}$$

where A = is the maximum displacement of the TE from the equilibrium position. The characteristic lengths used in this project are the maximum thickness $\mathcal{D}$ and the chord length of the foil $\mathcal{C}$. Note that, when the motion involves rotation e.g. in pure pitch, A is influenced by the location of the pivot point. This is characterised by $\mathcal{P} = x/\mathcal{C}$ which is

the non-dimensional distance between the leading edge (LE) and the pivot point along $\mathcal{C}$.

For a tandem configuration the distance between the TE of the front foil and the LE of the hint on the streamwise direction is expressed by the interfoil spacing $\mathcal{S}$ which is non-denationalized in a similar fashion to A_L as:

$$\mathcal{S}_L = \frac{\mathcal{S}}{L} \tag{2.4}$$

The load coefficients C_i can be expressed by simply dividing the hydrodynamic loads with the dynamic pressure of the freestream and a power of the chord length accordingly (second power for forces and third power for moments). In this study, the flipper experiences thrust $F_x(t)$ towards the forward direction, side-force $F_y(t)$ towards the transverse, and a moment $M_z(t)$ at the pivoting point. Due to the oscillating kinematics implemented here, the above quantities vary periodically through the flapping cycles and therefore integration is needed to calculate average values.

In 2.5 we see the coefficients of thrust (C_t, i), lift (C_l, i) and moment (C_m, i) for a two dimensional domain. These can refer to either the single, the fore or the back foil, described by their respective subscripts s, f or b. For the three dimensional counterparts the dynamic pressure equation (denominator) includes an extra, length term to account for the area of the wing (instead of just the $\mathcal{C}$) and the subscripts are in capital letters (see Chapter **??**). Time averaged quantities are presented with a bar superscript to distinguish them from the instantaneous ones, while the relative coefficients are denoted with a star superscript. These relative load coefficients enable us to quantify the gains of the tandem configuration as expressed by the fraction of the back foil coefficient over the coefficient of the single (front) foil.

$$C_t, i = \frac{F_x, s}{0.5\rho U_\infty^2 \mathcal{C}} \quad , \quad C_l, i = \frac{F_y, s}{0.5\rho U_\infty^2 \mathcal{C}} \quad , \quad C_m, s = \frac{M_z, i}{0.5\rho U_\infty^2 l\mathcal{C}} \tag{2.5}$$

The propulsive (hydrodynamic) efficiency (η) is defined as the output power over the input power such that $\eta = \frac{TU_\infty}{P}$, where $P =$ the power input and can be defined as:

$$P(t) = F(t)\dot{h(t)} + M(t)\dot{\theta(t)} \tag{2.6}$$

Alternatively the input power can be expressed by the integration over the foil, of the local fluid forces times the local velocity vector (Weymouth, 2016):

$$P(t) = \int_{i=0}^{s} \vec{f_i}\vec{u_i} \tag{2.7}$$

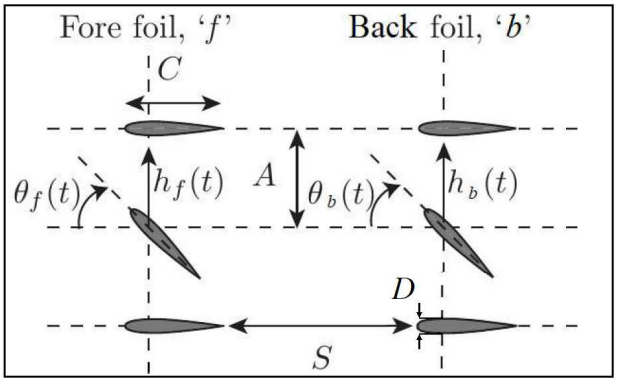

Figure 2.1: Basic geometric and kinematic parameters of a tandem configuration undergoing harmonic heave to pitch coupling. Redrawn from Muscutt et al. (2017b).

It is common for high efficiency regimes to not coinside with high performance (maximum force generation) (Muscutt et al., 2017b), which underlines the need for careful and flexible design of biomimetic propulsors.

2.2 Kinematics and Coordinates Definition

Before analysing the various factors that influence single and tandem foil propulsion, we need to set up the coordinates and terminology with respect to the foil motion. In 2D domains the motion can be a pure rotation, translation towards the x and/or y-axis, or a combination of the above. For the greater part of this study, we focus on simple *harmonic* motions of pure heave, pure pitch, and pitch and heave coupling (see figure 5.2). This harmonic nature of heave and pitch enables us to express the coupling as a superposition of the two kinematic components:

$$y_s(t) = y_h(t) + y_\theta(t) \quad where:$$

$$y_h(t) = h_0 \sin(2f\pi t) \quad , \quad y_\theta(t) = (1-\mathcal{P})\mathcal{C}\sin(\theta(t)) \quad and: \tag{2.8}$$

$$\theta(t) = \theta_0 \sin(2f\pi t + \psi)$$

where subscript s refers to the single foil configuration while the subscripts h and θ refer to the heaving and pitching component respectively.

The instantaneous angle of the foil due to pitching is expressed as the harmonic $\theta(t)$ with the h_0 and θ_0 being the amplitudes of pure heave and pure pitch respectively. In addition, the heave to pitch phase difference is set as $\psi = 90°$, which is shown to maximize the propulsive efficiency of the foil within the frequency range of interest (Platzer and Jones, 2008).

Another important kinematic parameter in coupled motions is the effective angle of attack $\alpha_{eff}(t)$, which is the summation of the instantaneous pitch angle $\theta(t)$ and the heave induced angle of attack. Thus for $\psi = 90°$ the amplitude of $\alpha_{eff}(t)$ is:

$$\alpha_0 = \arctan \frac{2\pi f h_0}{U_\infty} - \theta_0 \tag{2.9}$$

where $2\pi f h_0$ is the amplitude of dy_h/dt. Furthermore, the phase lag between the two foils is expressed as φ and will be referred to as simply the *phase*:

$$\begin{aligned} y_f(t) &= y_h(t) + y_\theta(t) \\ y_b(t) &= y_h(t+\varphi) + y_\theta(t+\varphi) \end{aligned} \tag{2.10}$$

where subscripts f and b denote the front and back foils respectively.

2.3 Single Flapping Wings

2.3.0.1 Overview

Every living organism whether swimming or flying, performs oscillatory motions to generate thrust and/or lift through body protrusions e.g. tail, fins, wings etc. These extremities have evolved into numerous variations both in terms of geometry and kinematics, in order to utilise fluid dynamics phenomena not clearly understood at present. In this chapter we do not attempt to cover every aspect of this wide topic, rather we try to set a basic understanding of flapping foil motion with focus on underwater applications, which is the main concern of our project. Due to a recent rise of interest in biomimetic propulsion, a great range of experimental and numerical research in flapping foil dynamics can be found in literature for a wide range of Reynolds numbers. More specifically it is shown that there is a direct link between Re and flapping configurations e.g. insect aerodynamics at low Re versus bird and bat flight strategies at high Re (Azuma, 2006).

The need for agility and fast response has led to complex 3 dimensional motions; one can notice at least 3 degrees of freedom for the flipper namely, rotation around the chord axis, rotation around the aerodynamic center axis (to change the angle of attack), and rotation normal to the chord axis (equivalent to plunging motion in 2D). In addition, actively controlled blade twist and foil curvature might be present to counter the velocity increase towards the tip of the flipper and to maintain the same angle of attack along the span, since many organisms utilise foil flexibility (Marais et al., 2012; Jaworski and Gordnier, 2015). As in most rotational mechanisms Coriolis forces are also common (Lentink and Dickinson, 2009).

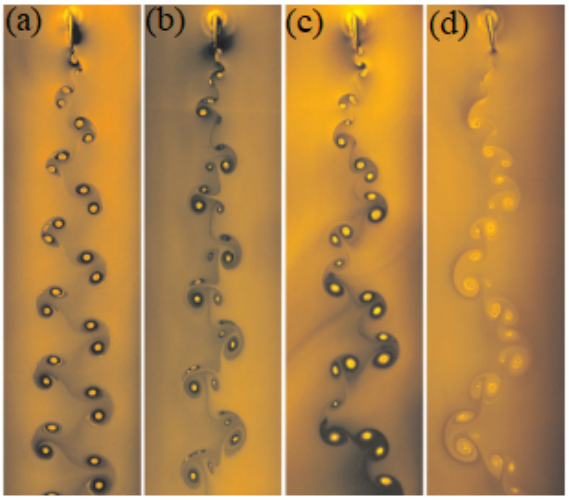

Figure 2.2: Vortex shedding patterns downstream of a flapping foil. Here the wakes are characterised according to the classification system of Williamson and Roshko (1988), where $mS + nP$ refers to m single vortices and n vortex pairs shed per oscillation period: (a) 2P wake, (b) 2P+2S wake, (c) 4P wake and (d) 4P+2S wake, redrawn from Schnipper et al. (2010).

Having mentioned the above, we should also note that the basic mechanics can be simplified as a coupled pitching and heaving motion when referring to a 2D representation. In a similar fashion to a 2D approximation of turbine flows, this approach does not take into account phenomena such as:

- tip vortices,
- spanwise development vortex structures upon the wing,
- shape and blending of vortex rings in the downstream wake,
- 3D design features e.g. taper ratio, AR, sweep and twist etc.

2.3.0.2 Thrust Generation

In order to understand the basic mechanisms that enable oscillating fins to produce thrust and/or lift, we need to focus on the fluid structure interactions (FSI) including the wake formation and vortex advection. Indeed, oscillatory motion is found to generate a great range of vortex patterns (see figure 2.2), which are of paramount importance in biological locomotion and manoeuvrability (Lighthill, 1969; Triantafyllou et al., 1993, 2000).

A classic example of this approach is the discovery of the *Benard von Kármán* wake. Today, it is well known that any stationary bluff body in 2D, surrounded by fluid within a range of Reynolds numbers, can cause the formation of alternating vortices in its wake

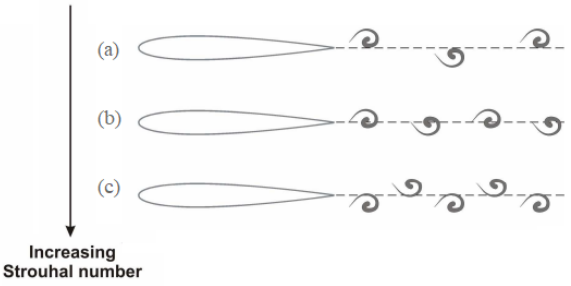

Figure 2.3: Wake development downstream of a flapping foil for increasing St: (a) Classic drag producing BvK wake, (b) neutral line and (c) thrust generating reverse BvK street, redrawn from Cleaver et al. (2012)

known as the *Benard von Kármán* (BvK) street. These vortices rotate in a sense that decelerates the flow with respect to the free stream which results in an average drag generation.

However, this is not always the case for an oscillating foil. Ignoring the 3D induced phenomena for a moment (as in high AR wings), we assume a flapping foil like the one shown in the figure 2.3. Whether this is a pure pitching, pure plunging or a coupled motion, at a certain St_A the oscillating frequency resonates with the natural vortex shedding frequency of the foil (Spiker et al., 2006; Godoy-Diana et al., 2009; Andersen et al., 2017). As the St_A increases, these vortices move towards the symmetry line of the wake creating a linear vortex pattern (Godoy-Diana et al., 2008a). Since the opposite rotation vortices cancel the effects of each other out, this pattern is neutral in terms of propulsion (no generation of thrust or drag). For a further St_A increase, the wake assumes a new alternating vortex pattern namely, the vortices rotate outwards and thus, accelerate the flow with respect to the free stream (thrust generation). In addition, literature suggests that within the range $0.2 < St_A < 0.4$ the propulsive efficiency maximizes (Anderson et al., 1998) which is consistent with observations in nature (Nudds et al., 2004; Taylor et al., 2003; Rohr and Fish, 2004).

Another way to describe flapping foil propulsion is through the changes within pressure/velocity field caused by vortex formation. Indeed, one of the key parameters in flapping propulsion is the formation of LE vortices (LEV). These are caused by an instantaneous separation commonly referred to as *dynamic stall*, that occurs due to the abrupt change of the angle of attack during a stroke. LEV increase the local flow velocity and a suction force is generated at the frontal area (see figure 2.4), resulting in instantaneous lift and thrust generation. Thus, it has been reported that large LEV can contribute to the overall thrust production of the system (Park and Choi, 2012).

Different types of motion result in LEV and TE vortices (TEV) of different sizes so that the overall thrust strongly depends on the underlined kinematics. More specifically, pure plunge is related to deep dynamic stall with strong LEV being shed and convected downstream adding to the total thrust of the configuration. On the other hand, coupled

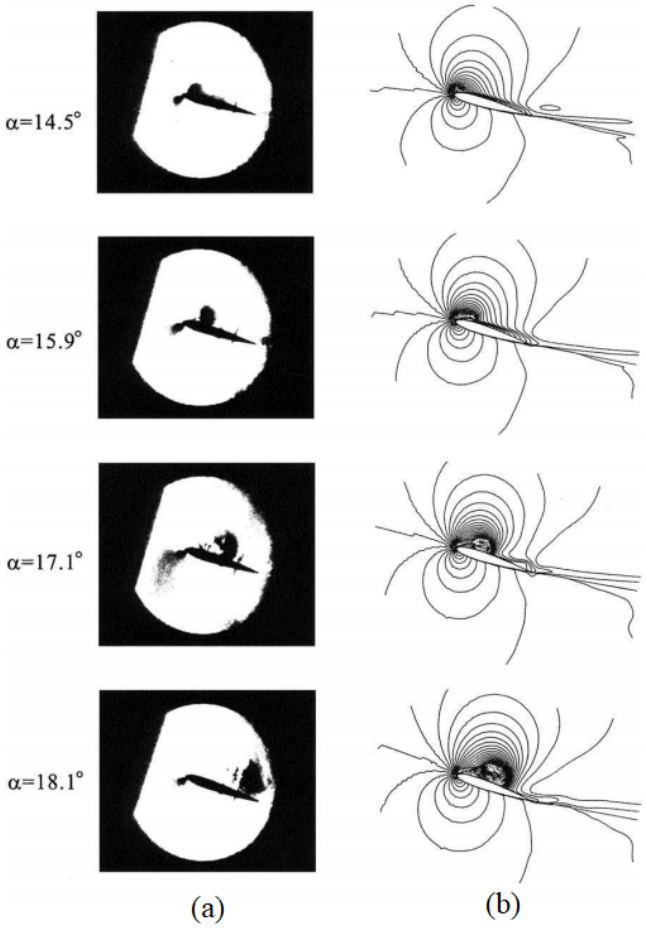

Figure 2.4: Comparison of (a) experimental and (b) numerical flow patterns around NACA0012 airfoil oscillating in pure pitch. The motion is characterised by a harmonic function of the angle of attack $\theta(t) = \pi/18 + \pi/18 \cdot \sin(\omega t)$. Here $U_\infty = 102.9\ m/s,\ Re = 10^5,\ \omega = 0.10\ rad/s$. (Isogai et al., 1999)

motions results in lower effective angle of attacks compared to pure heave and thus, into a shallow dynamic stall and mild flow separation, with no significant vorticity at the LE (Ol et al., 2009).

Here it should be noted that the majority of natural flipper based swimmers engage in some short of coupling between different harmonic motions to produce adequate propulsion (Jones et al., 2001; Wiens and Hosoi, 2018). This information provides a great insight towards the optimisation of flapping foil configurations (Bandyopadhyay and Leinhos, 2013).

2.3.0.3 Lift Generation: The Wake Deflection Approach

A variety of strategies and mechanisms enable lift generation in nature. The existence of a bias angle of attack (or foil camber) with respect to the freestream is a typical bird strategy to produce adequate amounts of lift (Read et al., 2003). In addition birds can

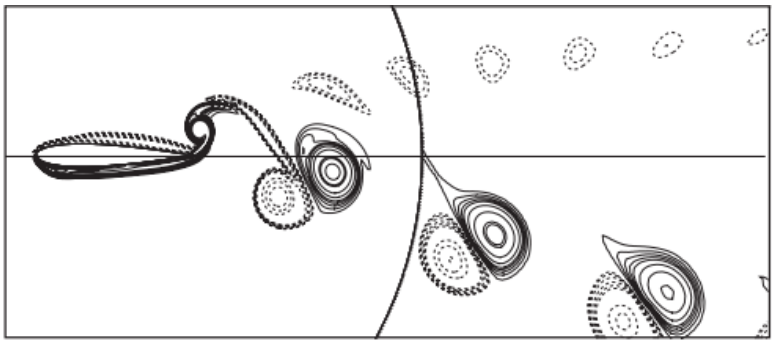

Figure 2.5: Instantaneous vorticity contours for the two-dimensional flow past a flapping foil at $Re_C = 1500$ with nondimensional amplitude $A_D = 2.13$. The boundary between the fixed and moving grids is shown with a curved solid line, redrawn from Deng and Caulfield (2015)

generate lift by varying the frequency and flapping amplitude which leads to a downward wake deflection.

Wake deflection has been reported for flapping foil configurations both experimentally (Jones et al., 1998; Buchholz and Smits, 2008; Von Ellenrieder et al., 2008; Godoy-Diana et al., 2008a) and computationally (Jones et al., 1998; Lewin and Haj-Hariri, 2003), even for zero foil camber or bias angle. The phenomenon has also been observed in oscillating cylinders due to the correlation of natural and forced vortex shedding (Couder and Basdevant, 1986). This asymmetry marks the generation of lift or down-force (depending on the sign of the deflection angle) together with thrust. A simplified physical explanation is that under certain $f - A$ combinations the circulation of a pair of counter rotating vortices is strong enough to form a dipole downstream of the TE. Above a certain St_A, this dipole has enough momentum to deviate from the main vortex street signalling the start of the deflection. Here it should be noted that these deflections have been observed in a range of A and f that partly coincides with the optimal St_A range mentioned above. Thus it is at least possible that both flying and aquatic animals are well aware of wake deflection and intentionally utilise or avoid this phenomenon to enhance they flying capacity (Godoy-Diana et al., 2008a).

2.3.0.4 Aspect ratio

In a three dimensional flow the aspect ratio (AR) is among the most influential parameters of flipper propulsion. By definition $AR = W^2/G$ (where W is the wingspan and G is the area) and can be interpreted as a measure of the flipper's slenderness (Von Mises, 1959). Long narrow wings like those of wind-turbines or commercial aircraft reach high values of AR, while gas turbine blades and fighter wings have significantly lower AR.

Induced vorticity from the tip and root of the wing has little effect on high AR configurations and they can be examined through *Quasy* $2D$ analysis, whether stationary

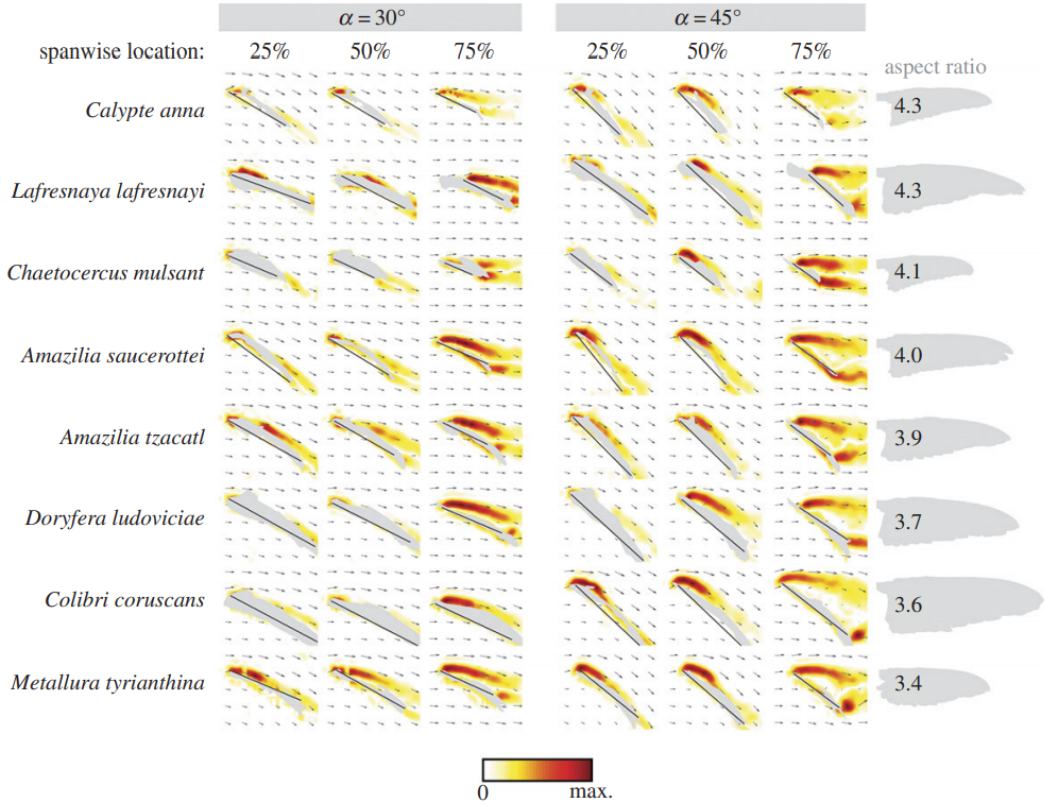

Figure 2.6: PIV obtained flow fields around wings of eight hummingbird species at two downstroke angles of attack: $\alpha = 30^o$ and $\alpha = 45^o$ (ranked for wing aspect ratio). The vorticity and velocity fields shown represent the average for 25 phase-locked snapshots at three stations along the wing: 25%, 50% and 75% wing span (from root to tip). Grey masks cover areas in which velocity data could not be obtained due to reflection of laser light at the surface; straight black lines are plotted between the LE and TE. (Kruyt et al., 2014).

or flapping as the ones mentioned above (Koochesfahani, 1989; Anderson et al., 1998). Moreover, weak tip vortices mean lower drag penalty in gliding/cruise. On the other hand, low AR fins are more robust and manoeuvrable and therefore more preferable in turbomachinery and military aircraft. In the case of flapping foils, decreasing span to chord ratio increases three-dimensional effects, alternating significantly the wake pattern. Complex vortex formations e.g. horseshoe vortices, are augmented by incoming root and tip vorticity, breaking the wake symmetry (Von Ellenrieder et al., 2003; Buchholz and Smits, 2006, 2008).

The importance of AR in propulsion and manoeuvrability is evident in many natural configurations. Gliders like albatross possess high AR wings many times longer that their frame, capable of energy efficient flight while predators like eagles or humpback whales poses shorter designs to increase agility. In addition AR is a key component of aerodynamic efficacy in hummingbirds, the only known bird species capable of hovering. More specifically, research suggests that although the link between AR and the forces

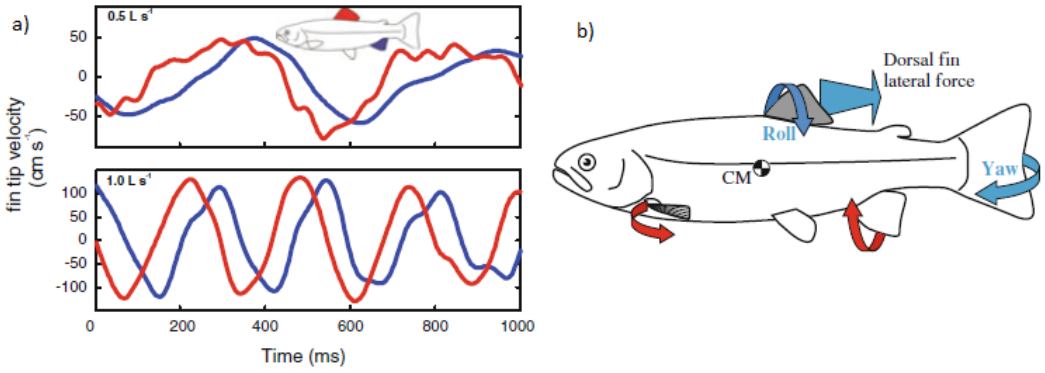

Figure 2.7: (a) Velocity time history of the dorsal and anal fins while swimming at to different speeds. The combined function of these fins impacts the overall propulsive load of the fish as well as the generating torques. (b) Review of the behavior of various fins and their impact in the orientation of the fish body (Lauder, 2015).

acting on the wing is weak, there is a strong correlation between AR and power consumption (Kruyt et al., 2014). PIV experiments reveal that the cause of this behaviour is the stabilising effect of LEVs (see figure 2.6).

2.4 Tandem Flapping Wings

2.4.0.1 Definition

An in-line flapping configuration is one where a flapping fin (or one hydrofoil in a 2D domain) is placed downstream of another. Although, the physics regarding the fore flipper/hydrofoil is virtually the same, the flow-structure interaction differs significantly for the aft foil. Here the foil faces an accelerated inflow of opposite rotating vortices as a result of the reverse BvK street of the fore foil. Therefore, one can expect a variation of important hydrodynamic parameters namely, the inflow angle, angle of attack, average ambient flow velocity, level of turbulence etc.

Tandem or quasi-tandem configurations are quite common in nature. It is believed that the 'V' formation of bird flying groups serves as a way to recuperate (Azuma, 2006) some of the upwash generated by the wing tip vortices of the front bird (Azuma, 2006; Spedding, 1987). In addition, flying insects (e.g. dragonflies) utilise a pair of tandem wings to achieve high performace at low Re (Saharon and Luttges, 1987). It should be noted that dragonflies in particular are able to oscillate their wings in and out of phase either for manoevering (Alexander, 1984) or efficiency purposes (Thomas et al., 2004). Furthermore, fish are partly utilizing tandem configurations through the interaction of the *caudal* and *dorsal* fins although not independently of each other (Bandyopadhyay and Leinhos, 2013; Lauder, 2015; Akhtar et al., 2007)

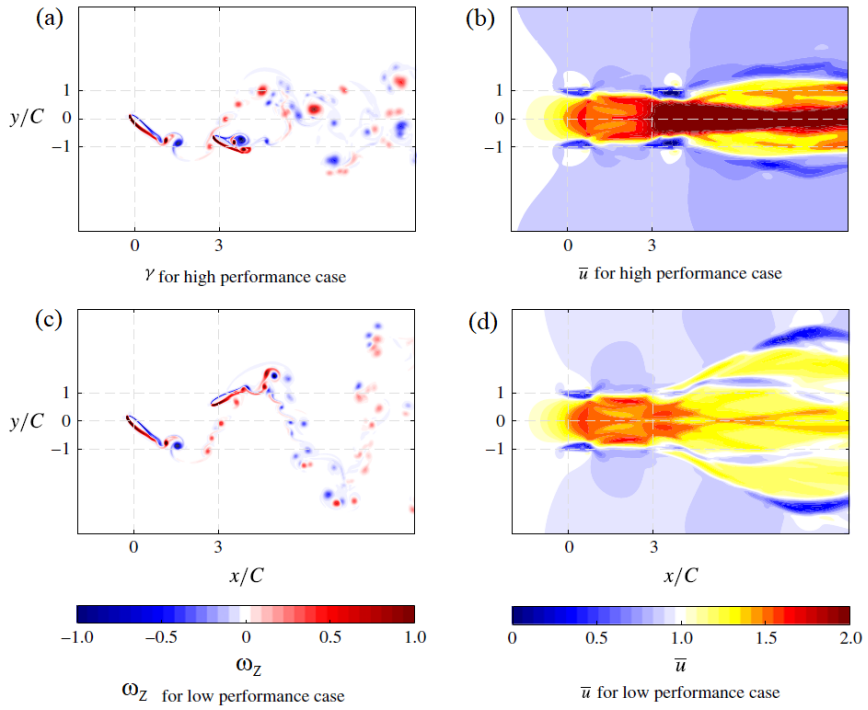

Figure 2.8: Contour plots of instantaneous vorticity magnitude (ω_z) and time-averaged streamwise velocity field ($\tilde{u}$) for the single, high-performance $\mathcal{S} = 2$, $\phi = 7\pi/4$ and low-performance case $\mathcal{S} = 2$, $\phi = 3\pi/4$,all at $St_A = 0.4$. For the vorticity fields the fore foil is midway through the upstroke, clockwise vorticity is indicated with blue and anticlockwise with red. In all figures, the vertical grid lines show the locations of the quarter-chord points of the fore and hind foils, and the horizontal grid lines show the midline of the domain and the upper and lower limits of heave motion. (Muscutt et al., 2017b)

Research indicates that the inter foil phase angle ϕ and the inter foil spacing (S) are the most crucial factors influencing the aft foil's thrust generation (Broering and Lian, 2012b; Lian et al., 2014; Kinsey and Dumas, 2012; Broering and Lian, 2012a; Kumar and Hu, 2011). It has been found that certain combinations of the above parameters for flapping foils under the same kinematics result in higher values of thrust for the hind foil with respect to the fore. Following the terminology of previous research (Muscutt et al., 2017a,b) we will refer to this phenomenon as performance augmentation.

2.4.0.2 Phase angle

The convection speed of the vortices that the fore foil has shed is strongly affected by the vortex strength, incoming disturbance, St, Re etc. By recording the oscillating history of the foil it is easy to accurately predict vortex propagation for a couple of chord lengths downstream, until 3D effects become significant. Thus we can influence the interaction between the incoming vortices and the aft foil by utilising the hysteresis between the

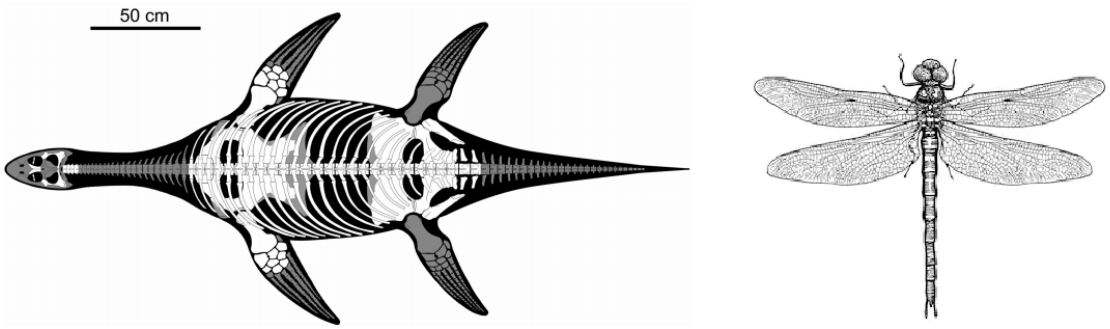

(a) (b)

Figure 2.9: (a) Full-body reconstruction of *Tatenectes laramiensis*, from the Upper Sundance Formation (Oxfordian) of Wyoming. Total reconstructed body length is just under 3m (O'Keefe et al., 2011). (b) Vintage sketch of a dragonfly, unknown artist.

two motions, per given space. In other words, active control of the front wake can be performed through careful arrangement of the inter foil phase angle ϕ.

Intentional phase lag within tandem configuration is prevalent in nature. Indeed, ϕ has been observed to improve the propulsive characteristics of in line insect wings by generating almost 22% more thrust than the standard single wings (Usherwood and Lehmann, 2008a; Lehmann, 2009). This is achieved by the back wing partly absorbing the wake swirl of the incoming jet, so that the overall momentum waste is minimized.

2.4.0.3 Spacing

For insects like dragonflies, spacing of in-line wings is almost zero (Usherwood and Lehmann, 2008a), yet plesiosaur fins were apart for at least 3 to 5 chord lengths. Distances higher that these result in quasi single foil flapping at low Re (Lehmann, 2009).

Although spacing between flippers in nature is driven by many factors, including the body length, it plays a key role in improving efficiency since it implicitly influences the interaction between the hind foil and the wake of the fore foil. Vortex convection rate is essentially a measure of velocity. Therefore, in order to utilise its effects in a beneficial manner we either need to adjust the foils according to time (via ϕ) or according to the space between them.

2.4.0.4 Performance augmentation

Today, most published work in the field analyses phase effects (Rival et al., 2011; Lian et al., 2014), phase and frequency (Broering and Lian, 2012a), or spacing and frequency (alternatively Strouhal number, St) (Kinsey and Dumas, 2012). Others focus on phase and spacing, but for one flapping frequency (Broering and Lian, 2012a; Kumar and Hu,

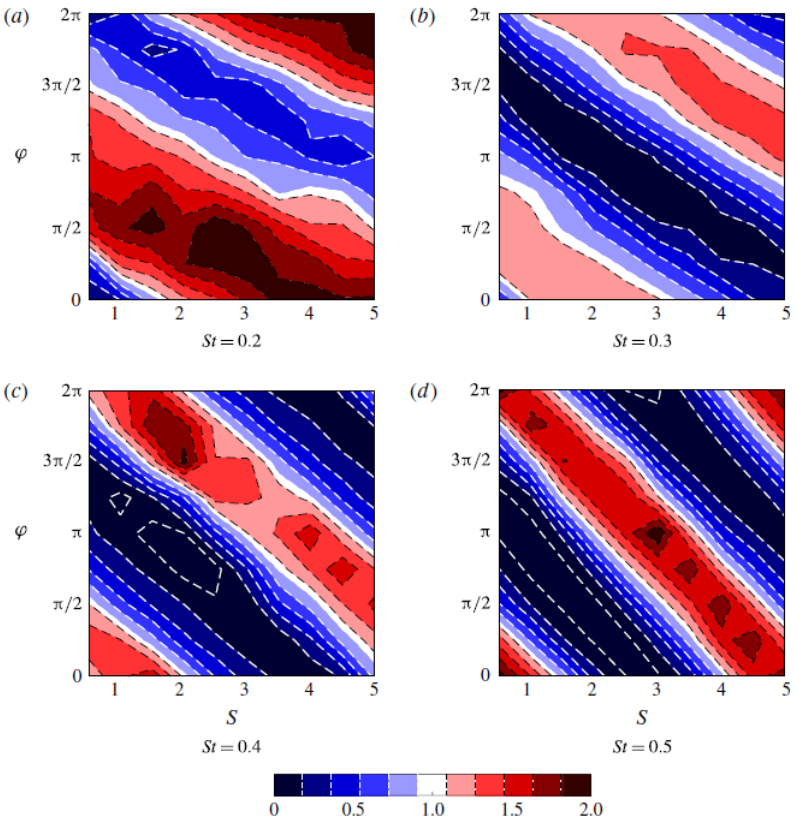

Figure 2.10: Contour plots of the measured mean thrust coefficient of the hind foil with respect to the single foil ($\widetilde{C_{t,h}}^*$), for all phase (ϕ) and spacing ($\mathcal{S}$) combinations over four Strouhal numbers, each calculated using 80 tandem-foil simulations. Red is high thrust and blue is low thrust, white represents the value of a single foil. (Muscutt et al., 2017b)

2011; Boschitsch et al., 2014; Gong et al., 2015, 2016). In addition, two studies have analysed both spacing and phase at various oscillating frequencies,(Broering and Lian, 2012a; Muscutt et al., 2017b), although to the authors understanding only the latter presented a detailed parametric study of all three factors.

As we can see in figure 2.10, when in a tandem configuration the hint foil can generate as much as two times the thrust of the single (front) foil. It is also clear that improper parametric combinations result in thrust even lower than in the case where the foil was single. Areas of thrust augmentation expand in parallel diagonal bands where the maximum thrust enhancement is concentrated in dark red peaks. These peaks are linked to the performance of the front foil; thrust augmentation maximizes when there is a lot of energy dissipation in the wake of the front foil and vice versa (Muscutt et al., 2017b). One can note that, adequate propulsive augmentation occurs for many parameter combinations, which demonstrates the versatile and adaptive nature of the configuration.

A closer look on various instances of the flowfield during a stroke of the tandem configuration reveals the mechanism of propulsion enhancement. Looking at the vorticity field for the high-thrust tandem case (see figure 2.8 b) one can notice that the aft hydrofoil sways into the high velocity serpentine formed between the incoming vortices of the front. Thus, the effective angle of attack is increased and with it, LE separation. This leads in turn to stronger vortices shed downstream. The mixing of the front and back foils vortices forms a broad propulsive jet known as *double BvK street*. That is the main difference between a single foil wake and an enhanced wake under a tandem configuration and explains the large augmentation achieved by the hind foil (Muscutt et al., 2017a,b). On the other hand, in the case of the low-thrust test (figure 2.8 a) the aft foil collides with the incoming vortices. This significantly weakens the wake, minimising, or even cancelling the benefits of the proposed configuration.

2.5 Plesiosaur considerations

In a similar fashion to land based, four legged animals, the Plesiosaurs' flippers can be split into some basic groups. Thus as we see in A of 2.11 a typical Plesiosaur flipper consists of the humorous, ulna and radius, the wrist bones, metacarpals (palm bones), and finally the phalanges (fingers).

As in most aquatic reptiles the flipper's bones here are vertically flattened, but stretched span-wise,so that the cross section resembles a hydrofoil. More specifically, contemporary research suggests that the profile that better mimics the flippers' cross section is the Eppler 387 (Muscutt et al., 2017b). Most of the middle section bones are short and round forming a relatively stiff body. Yet the wrist and finger bones are slender quasi-cylindrical objects. The chord wise variation of these fingers' length results in highly tapered and flexible flippers (Muscutt, 2017).

2.5.0.1 Flipper geometry

In 2.12 we see that the flipper's AR varies not only among various Plesiosaurs' subspecies but also with respect to its location on the animal's body. More specifically there is a clear difference between two distinct groups, the *plesiosauromorphs* which possess high AR flippers and the *pliosauromorphs* where the opposite occurs (Muscutt, 2017). It is generally accepted that the first group demonstrated short bursts and high manoeuvrability, whilst the second group was more focused on efficient cruise (O'Keefe, 2001). This statement is also in agreement with the distinction among contemporary birds as mentioned in 2.3.0.4. Another important feature shown in 2.12 is the ratio between the hint and fore flipper's AR. Notably the back flippers of high AR configurations are often longer and more slender than the fore ones. The reason behind this incident hasn't been

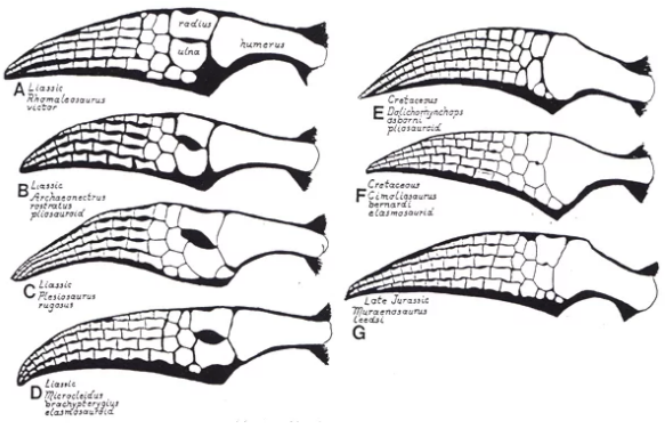

Figure 2.11: Anatomy and external geometry of various Plesiosaurs' flippers. (Bakker, 1993)

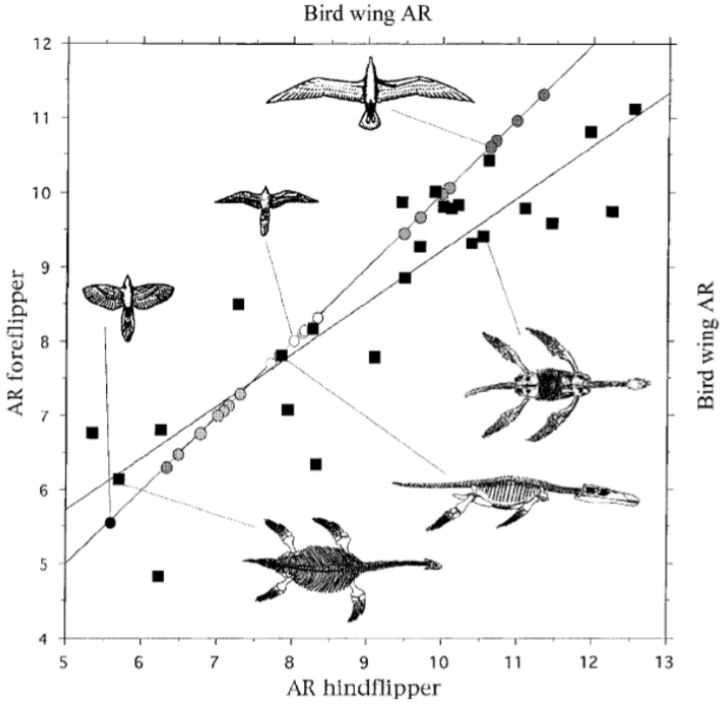

Figure 2.12: AR comparison between various birds and Plesiosaur species for both fore and hint flippers (O'Keefe, 2001)

clarified yet. However, to a certain extent these differences can be contributed to the statistical variance of the sample (O'Keefe, 2001).

2.5.0.2 Underwater flight in tandem

Any swimming technique involving at least partly heaving flippers is referred to as *Underwater flight*. Although a bird like motion of the fore flippers was proposed earlier (**?**), it was Robinson and JA (1975) that first suggested an identical *flying pattern* for the entire tandem configuration . Analysing the musculature and geometry of contemporary aquatic propulsors found in nature, she argued that other types of motion e.g. rowing, would require paddle like limps. Yet as mentioned previously the plesiosaurs' flippers are highly tapered resembling other underwater fliers. Among them the sea lion seems to demonstrate the closest contemporary approximation of the plesiosaur swimming pattern due to skeletal and muscle similarities (Godfrey, 1984). More specifically the pectoral girdle in both cases stretches horizontally enabling a lift based locomotion (Robinson and JA, 1975; Robinson, 1977).

2.5.0.3 Plesiosaur Phasing

Early considerations about the Plesiosaurs' phasing strategies can be traced back to the 1980's (Tarsitano and Riess, 1982; Frey and Riess, 1982). It was suggested that the back and fore flippers were performing opposite motions which can be mathematically interpreted as an 180 *degrees* phase angle. A simple yet straight forward approach of the topic can be given through the *action* and *reaction* concept. Like a propeller when a flipper pushes its surrounding fluid, an equal opposite load will be experienced by the plesiosaur's body. Thus if the flippers are oscillating *in phase* ($\phi = 0$) the plesiosaur's body will engage in a pure heaving motion. However, if the flippers are oscillating *out* of *phase* ($\phi = \pi$) the body will rotate with respect to the lateral axis due to the eccentric placement of the flippers generating a pure moment. It is therefore suggested that any other phase option leads to the body following a superposition of these two extremes also known as *porpoising* (Newman and Tarlo, 1967; Halstead, 1989).

A number of parameters such as poor fossil quality, solver and experimental setup limitations, absence of similar species in the modern world etc. make it difficult to provide the reader with the exact swimming patterns and overall hydrodynamics of the plesiosaurs´ flippers. Yet an optimisation of the tandem configuration kinematics and geometry in terms of propulsive performance offers a reliable tool. Nature always evolves towards more efficient designs and therefore if an option is considered optimal in engineering it is likely beneficial within the wildlife.

Towards this principal, a recent study was conducted by utilising force response and flow visualisation on a *robotic* plesiosaur (Muscutt, 2017). It was suggested that a frequent

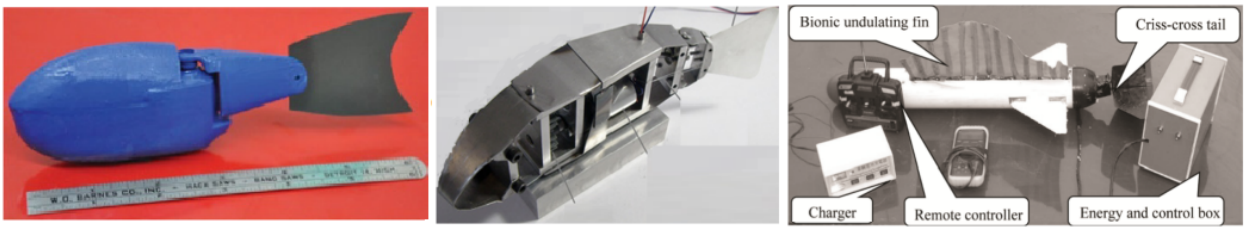

Figure 2.13: Examples of rigid link underwater bio mimetic propulsors: single link(a), multiple link (b) and fin actuators (c). Redrawn from Salazar et al. (2019)

change in phase was part of these animals' swimming strategy since optimal efficiency and thrust augmentation occur at different ϕ - S combinations for different swimming conditions (Muscutt et al., 2017a).

2.6 UUV Applications

2.6.0.1 Background

The goal of this project is to gain a deep understanding of the tandem flapping foils configuration so as to utilise this knowledge for UUV applications. Flapping foils might be the efficient and agile alternative of the propeller (Thaweewat et al., 2018; Weymouth, 2016). To many, biomimetic foil propulsion could expand the marine drone's application range by increasing their speed and manoeuvrability without posing threat to the marine wildlife by direct impact or high pitch sound propagation. Thus, a brief summary of the present state of the art in the field is presented.

2.6.0.2 Rigid link actuators

The term is referred to any bio inspired propulsor e.g. flipper, tail etc. that maintains its size and shape. The moving parts are connected to rigid joints and are set to motion by electrical motors (Raj and Thakur, 2016). The simplicity of this concept has led to a plethora of designs, most of which belong to the following categories: single link, multiple link, and fin actuators.

A single link system (figure 2.13a) is often one that only enables the motion of tail on an otherwise rigid body frame. The motor is placed within the body or the tail. A major benefit of these systems is their simplicity. On the other hand, a multi-link actuator (figure 2.13b) enables more complex motions as it allows the change of the body curvature. Having a similar working principle to a spine, this system can be optimised by increasing the links of its configuration. Lastly, the fin actuators (figure 2.13c) utilize the

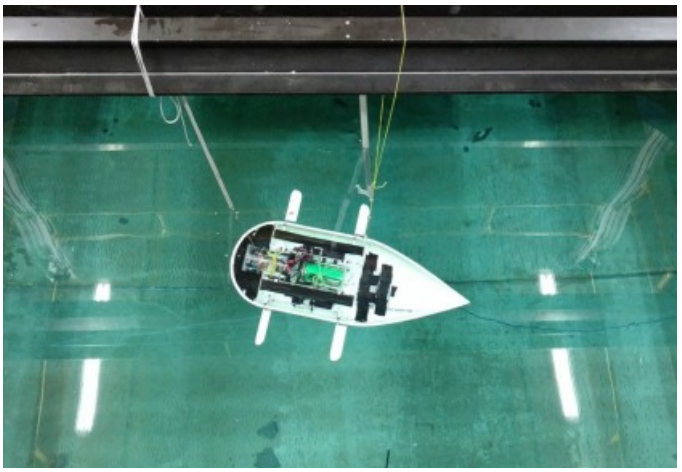

Figure 2.14: GDP Atlantis in the water (Weymouth et al., 2017).

extremities of the body (fins), either by generating a wavy motion along a multifaceted fin or by oscillating a number of rigid hydrofoils.

2.6.0.3 Multiple flipper systems

Most bioinspired flipper based configurations found in literature are rigid fin actuators, utilizing a single pair of flippers in turtle-like robots or combine the flipper action with the caudal fin in fish-like configurations.

For the purpose of analysing the impact of ϕ and gaits in tetrapodal swimming, (Long et al., 2006) built an underwater drone which utilises two hydrofoil pairs in tandem. These were pure pitching propulsors, without a heaving component, which is a weak thrust option as opposed to a coupled motion. They determined that the COT was lower on a two flipper configuration compared to the four flipper one, although the chosen kinematics undermined the capacity of back foil to enhance the overall propulsive mechanism.

A six flipper, torpedo shaped AUV (3 at the front and 3 at the back) was recently constructed by (Bandyopadhyay and Leinhos, 2013). However, the state of the art in the field is the AUV designed and manufactured by Licht et al. (2004) at the department of ocean engineering at the Massachusetts Institute of Technology, named *Finnegan*. This robot demonstrated unparalleled agility and a cruise speed of around 1 m/s (Licht et al., 2004).

One of the latest examples in the field, was constructed by Weymouth et al. (2017) at the University of Southampton as part of a group design project, on behalf of the Fluid Structure Interaction (FSI) group. The droplet shaped UUV is equipped with four independent rectangular fins. Heave motion is enabled by two electric motors while pitching is passive. The details of the structure can be seen in figure 2.14.

Chapter 3

Computational Methods

3.1 The solver

Computational fluid dynamics (CFD) enables researchers to explore flow related phenomena in a relative inexpensive and accurate manner. Thus, the amount of experimental research expected can be significantly reduced. The CFD solver chosen for this study is a FORTRAN-based script, called LOTUS, which can handle complex geometries and moving boundaries for a wide range of Reynolds numbers in 2D and 3D domains, by utilizing the Boundary Data Immersion Method (BDIM) Weymouth and Yue (2011).

The main feature of the Immersed Boundary methods (IB) is the addition of a force density factor into the Navier-Stokes equations, to account for the solid boundary motions Peskin (2002). This allows the use of a combined set of equations for the entire domain compared to the traditional two domain approach Weymouth and Yue (2011).

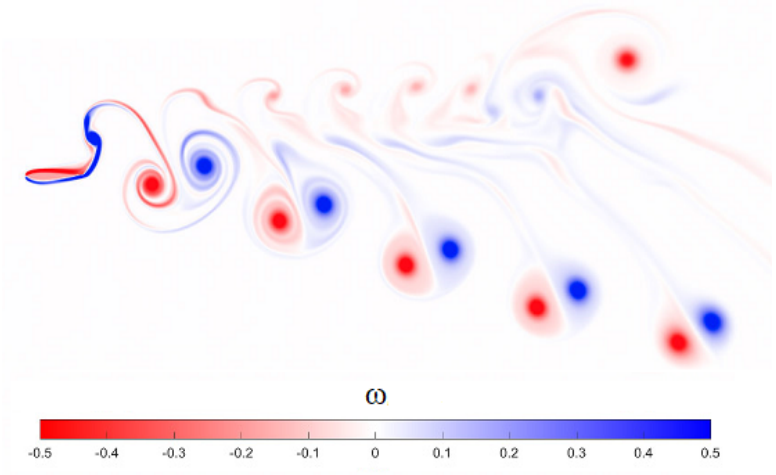

Figure 3.1: Contour plots of normalised instantaneous vorticity for a deflected wake.

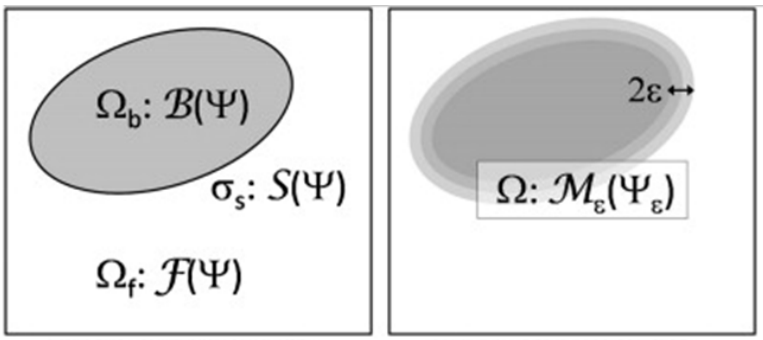

(a) Original P_0 problem (b) Modified P_ϵ problem

Figure 3.2: The BDIM consept. (a) Classic representation of a fluid-structure interaction problem with two domains and an interface with their respective governing equations B,F, and S.(b) BDIM model, reduced to one domain with a governing meta-equation M, constructed by convoluting and assembling the equations over a width ϵ and a smooth transition (Weymouth and Yue, 2011).

Further developments include direct estimation of the forcing function (Direct Forcing Methods) through the expected solid boundary velocity, but can lead to fictitious pressure fluctuations since the mass conservation of the solid is ignored Fadlun et al. (2000). Suggested solutions include, the introduction of ghost fluids Gibou et al. (2002) or ghost cells Mittal et al. (2008) (Sharp Interface Approach).

The BDIM is a hybrid approach inspired by Uhlmann Uhlmann (2005), but uses a distance formulation (general integration Kernel function) instead of Lagrangian points. It solves the modified mass and momentum conservation equations where both the velocity and pressure fields of the flow close to the solid are influenced by the fluid-solid interaction (see figure 3.2). Thus, simulations result in continuous pressure distribution even in unsteady cases e.g. flapping foils etc., whilst maintaining the ease of an IB method Weymouth and Yue (2011).

These equations have been implemented in a Cartesian grid i-Implicit Large Eddy Simulation (iLES) code using Euler explicit integration scheme with Huen's corrector. They are posed on a staggered mesh and central differences are used for all special derivatives except in the convective term which uses a flux limited QUICK scheme for stability. When the local flow is appropriately resolved, these equations automatically revert to a non dissipative (central difference) scheme (Weymouth and Yue, 2011).

3.2 Grid and domain analysis

The mesh configuration is a rectangular Cartesian grid with a dense uniform grid near the body and in the near wake, and exponential grid stretching used in the far-field (see figure 3.3). The numerical domain uses a uniform inflow, zero-gradient outflow and free-slip conditions on the upper and lower boundaries. Furthermore no slip boundary conditions

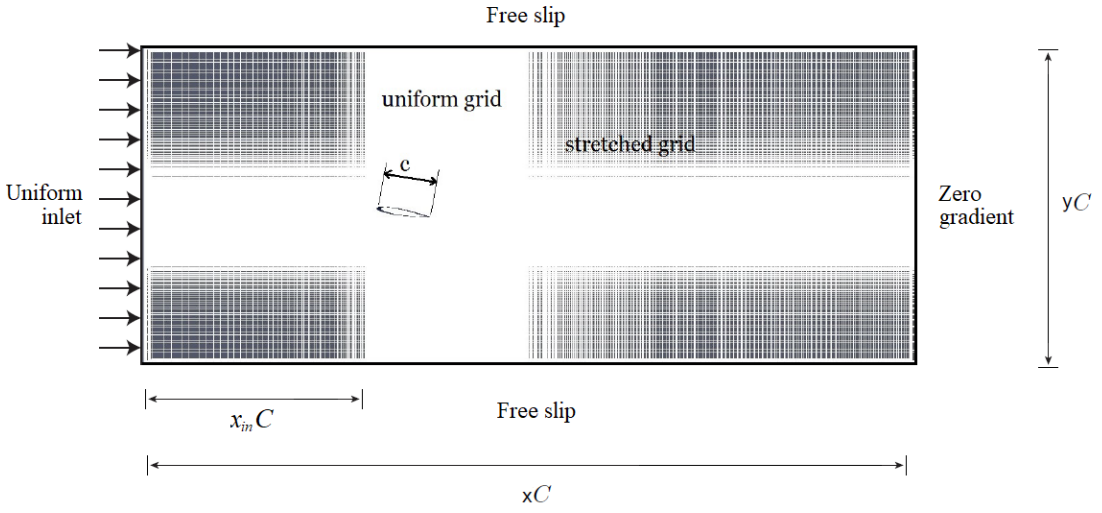

Figure 3.3: Domain configuration with the grid arrangement and the boundary conditions for a two dimensional single case. The overall dimensions together with the inlet spacing are measured in units of $\mathcal{C}$.

are used on the oscillating foil. Mesh density is expressed in terms of grid points per chord while the overall dimensions together with the inlet spacing are measured in units of $\mathcal{C}$.

Time convergence is enabled via the cycle to cycle comparison of the development of load coefficients e.g. C_t and/or C_l and the convergence of the cycled averaged coefficients e.g. $\widetilde{C}_t$-$\widetilde{C}_l$ through the accumulation of flapping cycles. As we see in the figure 3.4, cases of classic reverse *Bénard von Kármán* streets (see Chapter 2) are fully converged at about 10 cycles. More unstable phenomena, however, like the ones found in wake deflection test cases (see Chapter 5) required at least 30 cycles.

Grid dependency analysis is performed for both a single and a tandem foil configuration at $Re_{\mathcal{C}} = 1173$, for the domain size and kinematics derived from (Muscutt et al., 2017b) as this parametric combination is of utmost importance for this project (see Chapters 4 and 5). To ensure convergence we compare load coefficients e.g. $\widetilde{C}_t$ of increasing mesh density level to the ones of the subsequent finer grid. This can be expressed via the trendline of $\widetilde{Ct}$ versus grid density in a logarithmic diagram (see in figure 3.5). Here the relationship between the two parameters is roughly linear for both configurations indicating a power law. This is deemed beneficial as the *long tail* of such curves converges towards a straight line for large numbers in the x-axis (when plotted in a conventional non-logarithmic diagram). Alternatively, this can be seen via the decrease of the relative error of $\widetilde{C}_t$ for increasing mesh resolution in the tables 3.1 and 3.2 for tandem and single configurations respectively. For the purpose of this study, a uniform mesh of $\delta x = \delta y = \mathcal{C}/192$ is considered a sufficient trade off between the computational speed

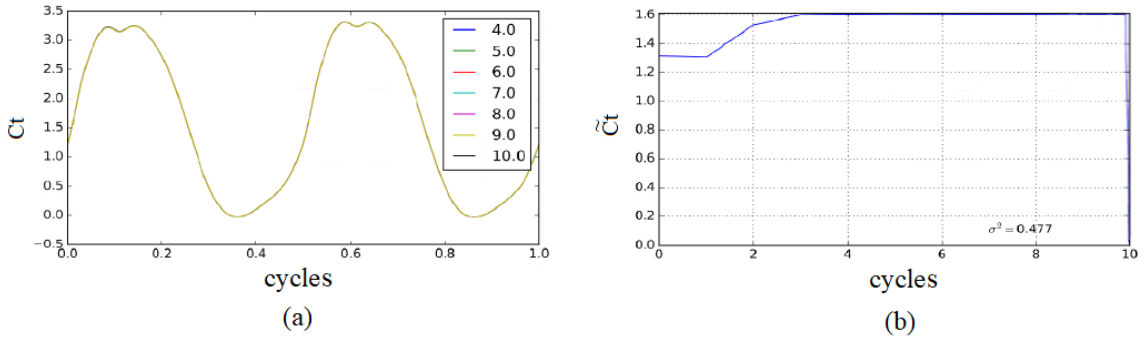

Figure 3.4: (a) Fluctuations of Ct from cycle to cycle. Notice the almost perfect overlap between the Ct of the cycles 4 to 10 due to the successful time convergence of the simulation. This is further verified by (b) the convergence of $\widetilde{C}_t$ within the first 3-4 cycles.

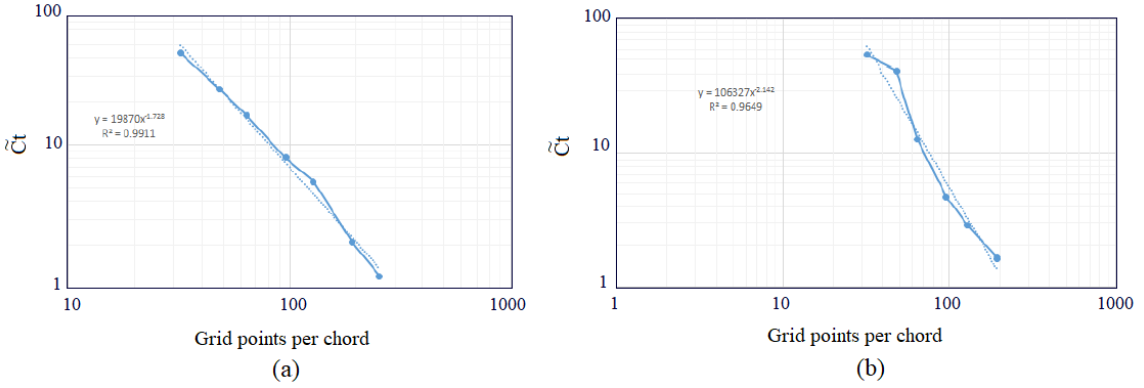

Figure 3.5: Grid convergence for (a) the single flapping foil and (b) the tandem flapping foils configuration in a log-log diagram. The relationship between the thrust coefficient and the grid resolution resembles a straight line, thus demonstrating a power law.

and the accuracy of the results. Thus, it should be assumed that all simulations presented in later chapters are conducted for this grid configuration unless specified otherwise.

Lastly, special attention has been paid to the size of both the uniform and the overall grid configuration to ensure a reliable wake development and the absence of non-physical phenomena such as blockage effects. This was enabled via a gradual increase of the dimension of interest until further increase did not alter the force coefficients or caused any obvious visual change of the pressure or vorticity field.

3.3 Validation

To ensure the reliability of the method, it is important to compare its results with published data of relevant literature. Indeed, BDIM has been validated for a wide range of $Re_{\mathcal{C}} \sim [10^3 - 10^4]$ and FSI problems such as towed cylinders (Weymouth,

Grid density	Thrust coefficient	error	relative error %
32	0.334	0.253	43.6
48	0.445	0.142	24.48
64	0.494	0.093	16.03
96	0.54	0.047	8.1
128	0.555	0.032	5.51
192	0.575	0.012	1.2068
256	0.58	0.007	1.2
512	0.587	0	0

Table 3.1: Table of $\widetilde{Ct}$ per grid density for a single flapping foil at $St_A = 0.4$, $A_C = 1$ and $Re_{\mathcal{C}} = 1173$.

Grid density	Thrust coefficient	error	relative error %
32	0.76	0.887	54.4
48	0.96	0.687	42.14
64	1.44	0.207	12.699
96	1.57	0.077	4.72
128	1.6	0.047	2.88
192	1.62	0.027	1.656
256	1.63	0.017	1.04
512	1.647	0	0

Table 3.2: Table of $\widetilde{Ct}$ per grid density for a tandem configuration at $St_A = 0.4$, $A_C = 1$ and $Re_{\mathcal{C}} = 1173$. Here $\phi = 270^o$ and $\mathcal{S}_C = 2$.

2014), boundary layer instabilities (Maertens and Weymouth, 2015), vorticity shedding of shrinking cylinders (Weymouth and Triantafyllou, 2012) and unsteady dynamics of perching manoeuvres (Polet et al., 2015). Moreover, a good agreement can be seen in figure 3.6 between single oscillating foil experiments derived from Anderson et al. (1998) and simulations performed by Muscutt (2017) where the same BDIM solver was used.

Finally, we compare our numerical data to the experiments conducted by Godoy-Diana et al. (2008a) regarding the wake transitions of a flapping foil undergoing pure pitch at $Re_{\mathcal{C}} = 1173$. Our simulations are conducted for the chosen uniform mesh of $\delta x = \delta y = \mathcal{C}/192$ and all other input parameters e.g. kinematics, St_D, $Re_{\mathcal{C}}$ etc. are identical to the experimental study. As we see in figure 3.7, the agreement between the two studies is satisfactory, which suggests that our computational solver is an accurate tool for the purposes of this project.

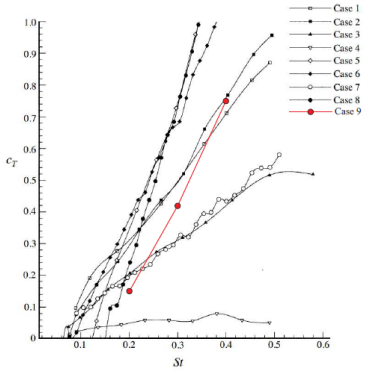

Figure 3.6: $\widetilde{Ct}$ as a function of St_A for single flapping foils undergoing harmonic motions. Cases 1-8 are derived from the experimental data of Anderson et al. (1998) while case 9 is derived from simulations conducted by Muscutt (2017). Note that case 5 and 9 have the same kinematics.

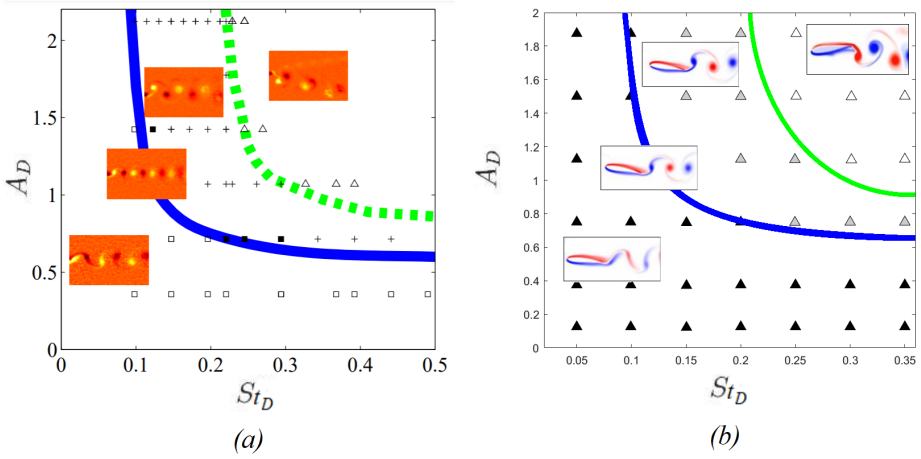

Figure 3.7: Transitions in the wake of a pure pitching flapping foil in the A_D vs. St_D map for $Re_C = 1173$ derived from (a) PIV experiments conducted by Godoy-Diana et al. (2008a) and (b) simulations conducted with LOTUS.

Chapter 4

Computational results: Towards a universal scaling law of the BvK reversal

4.1 Background

Almost all aquatic and flying animals generate thrust via the oscillatory motion of foil-like body parts e.g. tail, fin etc. Moreover flapping foil systems are often associated with high efficiency and strong side forces, ideal for manoeuvring (Read et al., 2003). Thus, many studies have focused on the analysis and implementation of these biological configurations into man made designs (Fish and Lauder, 2006; Triantafyllou et al., 2004; Wang, 2005) although the underlying physics is still not clearly understood.

Here we aim to determine the drag-to-thrust wake transition of these flapping mechanisms via the analysis of the vortex pattern development. Assuming foil undulations above the *lock in* frequency (Thiria et al., 2006; Vial et al., 2004) we observe at least three basic wake patterns (Von Karman, 1935): the classic *Bénard von Kármán* (Bvk) street where $U_{wake} < U_{\infty}$ (figure 4.1a), the neutral line where $U_{wake} \sim U_{\infty}$ (figure 4.1b) and the reversed BvK wake, where $U_{wake} > U_{\infty}$ (figure 4.1c). The latter is synonymous to the drag-to-thrust wake transition although a lag exists between this phenomenon and the foil's overall transition towards thrust. This is due to the fact that a weak velocity surplus cannot overcome profile drag or velocity fluctuations and pressure differences within the control volume(Streitlien and Triantafyllou, 1998; Ramamurti and Sandberg, 2001; Bohl and Koochesfahani, 2009).

As the driving factors of BvK reversal we typically consider the oscillating amplitude and the oscillating frequency f of the kinematics (Koochesfahani, 1989) . The former is expressed by the trailing-edge (TE) peak-to-peak amplitude A. In dimensionless terms

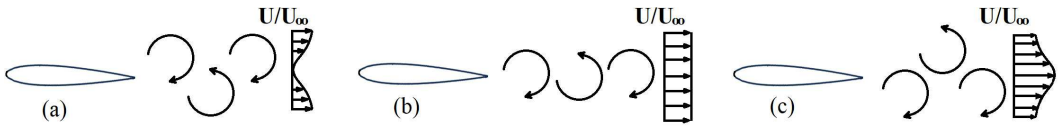

Figure 4.1: Drag-to-Thrust transition within the wake of a symmetric flapping foil. (a) BvK street, (b) Neutral line, (c) reversed BvK wake.

it is often normalised by the thickness D or the chord length $\mathcal{C}$ of the foil. In a similar fashion the frequency is often expressed as a reduced frequency $k = U_\infty/(f\mathcal{C})$ (Birnbaum, 1924), a thickness based Strouhal number $St_D = (fD)/U_\infty$ (Godoy-Diana et al., 2009) or a chord length based Strouhal number $St_\mathcal{C} = 1/k$ (Cleaver et al., 2012). Triantafyllou et al. (1991) suggested a modified amplitude based Strouhal number $St_A = (fA)/U_\infty$. By including both the frequency and the amplitude of oscillation, St_A can potentially characterise the BvK reversal by a single factor as opposed to k, St_D and $St_\mathcal{C}$. Studies of Anderson et al. (1998) and Read et al. (2003) showed that optimal efficiency occurs for a short range of $St_A \sim [0.2, 0.4]$. This was also supported by Taylor et al. (2003) and Triantafyllou et al. (1993) who observed that the majority of natural fliers and swimmers prefer to cruise within this range. According to Andersen et al. (2017), BvK reversal occurs at different St_A values for pure heave and pure pitch. Therefore, St_A cannot be regarded as an expression of self similarity.

The fundamental problem is that characterizing the motion only by the tail amplitude fails to capture the contribution of the other points of the foil. This becomes important when the heaving component is significant, resulting in the generation of strong *leading edge vortices* (LEV) which travel downstream and blend with the *trailing edge vortices* (TEV). Instead, we need to take into account the length of the entire path travelled in a period rather than the maximum distance from equilibrium expressed by A_D.

In this study, we formulate a novel length scale, which characterizes the Bvk reversal of harmonically flapping foils. We develop the new metric based on the chord-wise averaged path travelled by the foil, in order to determine BvK wake reversal for a vast range of harmonic motions.

4.1.1 Methodology

Two-dimensional simulations are conducted for a rigid NACA0016 profile ($D = 0.16\mathcal{C}$) and three basic harmonic kinematics (see figure 4.2): pure heave, pure pitch and heave-pitch coupling for a $\psi = 90°$, which is shown to maximize the propulsive efficiency (Platzer and Jones, 2008). Furthermore, the influence of different $\mathcal{P}$ is examined for pure pitch and coupled motions. Finally, we analyse the impact of different α_0 on the coupled kinematics.

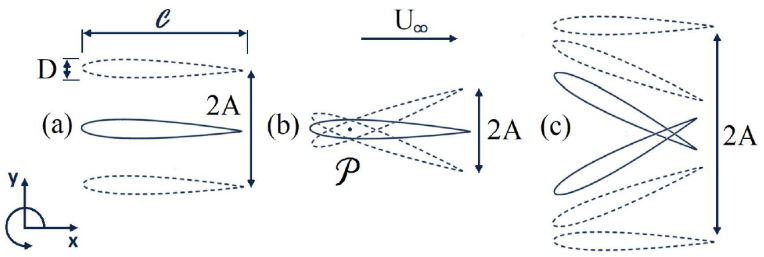

Figure 4.2: Foil kinematics, geometry and coordinate system. (a) pure heave , (b) pure pitch , (c) coupled motion.

A wide range of frequencies and TE amplitudes are tested in terms of St_D and A_D at a Reynolds number of $Re_{\mathcal{C}} = 1173$ to enable comparison with relevant literature (Godoy-Diana et al., 2009, 2008a; Andersen et al., 2017; Chao et al., 2019b). In particular, the drag to thrust transition is evaluated both in terms of a velocity surplus in the downstream wake and the overall $\widetilde{C}_t$ experienced by the foil.

4.2 Results and Discussion

4.2.1 Wake comparison of different kinematics

According to Godoy-Diana et al. (2008a), the Reynolds number range of naturally occurring flapping foils is $100 < Re < 10000$. In this study, most simulations are conducted for $Re = 1173$ to be within this range and to enable comparison with the experiments of Godoy-Diana et al. (2009). Additional simulations are conducted for selected cases at $Re = 11730$ to examine the higher Reynolds number effects. The pivot points tested for pure pitch and coupling are $\mathcal{P} = 0$ and 0.25. The coupled motion is also tested for three values of $\alpha = 5°, 10°$ and $20°$.

We analyse the wake patterns and resultant hydrodynamic loads for the above mentioned kinematics. Various stages of the wake development can be seen in figure 3 for pure heave, pure pitch for $\mathcal{P} = 0.25$ and coupled motion for $\mathcal{P} = 0.25$ and $\alpha = 10°$. The transition from the BvK (third row) to the neutral wake where vortices are shed in-line (fourth row) and later the reversed BvK (fifth and sixth rows) is in agreement with literature (Koochesfahani, 1989; Godoy-Diana et al., 2009; Andersen et al., 2017) . At lower $St_D - A_D$ combinations more complicated wake patterns e.g. 2P wakes (Williamson and Roshko, 1988) at the first row of figure 3 in accordance with those observed by Andersen et al. (2017) for wedge type foils. At such low $St_D - A_D$ combinations coupled motions are dominated by one of the two modes e.g. for $A_D = 0.4, St_D = 0.1$, the heaving contribution to the foil displacement is less than 5% for all the coupled cases studied. Therefore, a coupled motion around this region is acting more like a pure pitching case.

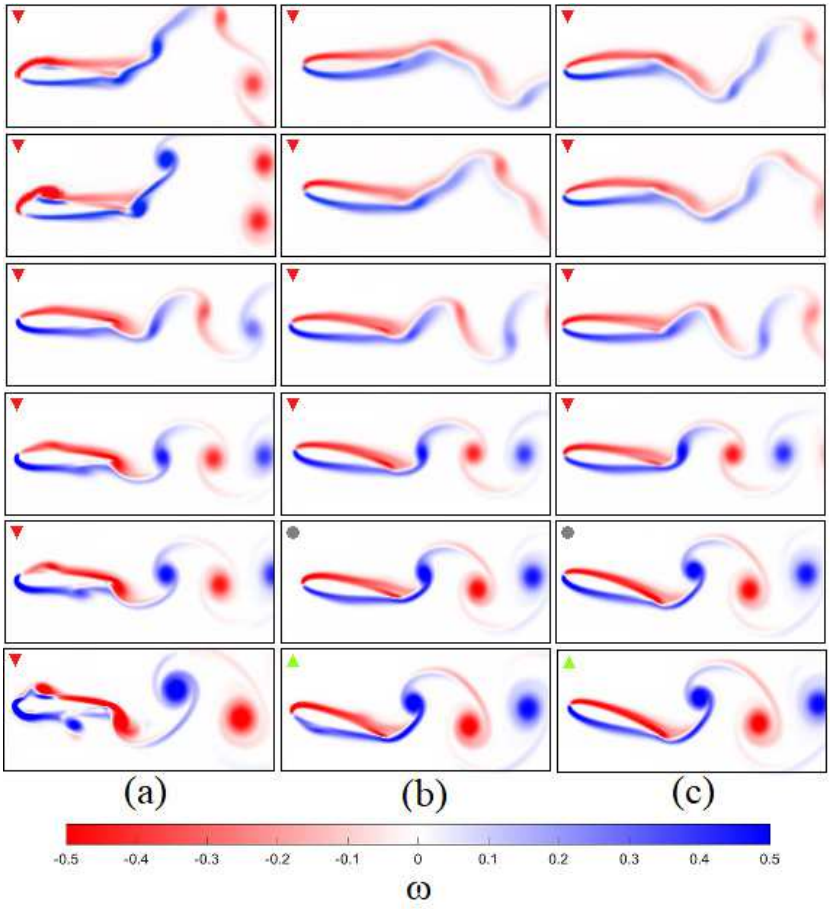

Figure 4.3: Contour plots of normalised instantaneous vorticity magnitude of the 30th cycle at $St_D = 0.15$ and $Re = 1173$, for (a) pure heave at $A_D \sim [0.5{-}0.1]$, (b) pitch at $\mathcal{P} = 0$ and $A_D \sim [0.82{-}1.3]$ and (c) coupled motion at $\mathcal{P} = 0, \alpha = 5^\circ$ and $A_D \sim [1.02 - 1.4]$. Drag regime red inverted triangles, neutral state grey circles, thrust producing flow green triangles.

Among the three kinematic test cases significant discrepancies can be seen in close proximity to the foil, most notably at the LE. The deep stall (high $\delta\alpha/\delta t$ across the chord) experienced by the pure heaving foil generates LEVs of sizes comparable to the TEVs which travel across the chord and blend with the wake. A closer look at figure 4.3c reveals that the coupled motion generates the smallest amount of dynamic separation among the three cases. Finally as seen in the last row of figure 4.3 even when the BvK street is fully reversed, some the cases exist within the drag producing regime. This lag is expected since a weak propulsive wake is not enough to overcome the profile drag or to compensate for the velocity fluctuations and pressure differences that exist within the control volume (Streitlien and Triantafyllou, 1998; Ramamurti and Sandberg, 2001; Bohl and Koochesfahani, 2009).

Figure 4.4 shows the best fit curve that isolates the neutral line (where $U_{wake} \sim U_\infty$), for the different harmonics. These best fit curves are reproduced in figure 4.5a in order to compare this neutral line across different kinematics. Although $St_D - A_D$ phase diagram

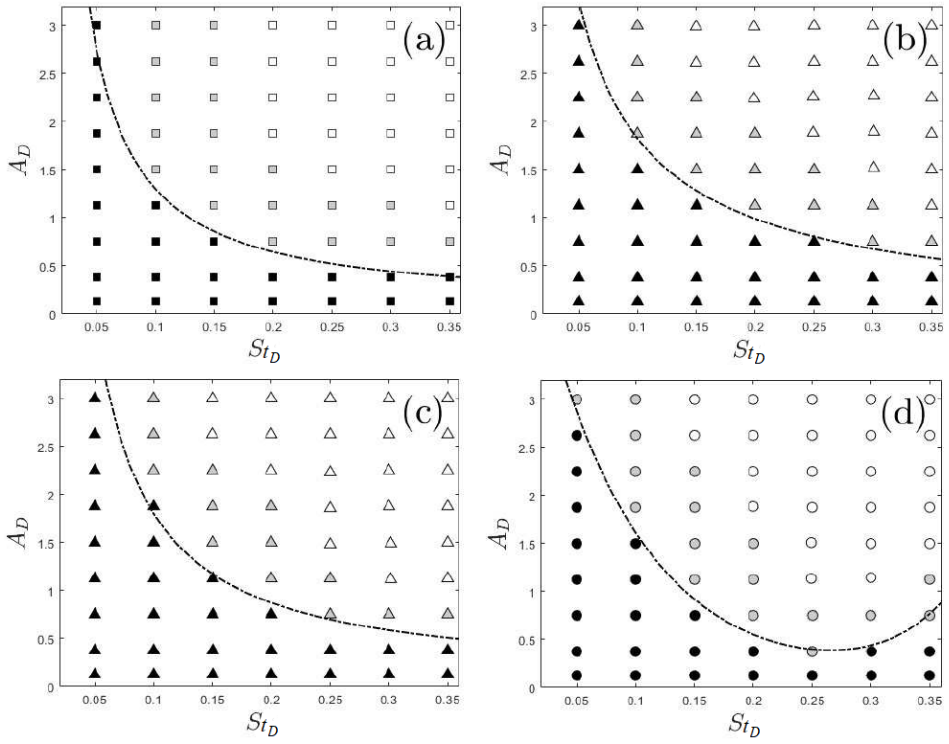

Figure 4.4: $A_D - St_D$ wake map for various kinematics at $Re = 1173$ for (a) pure heave, (b) pure pitch at $\mathcal{P} = 0.25$, (c) pure pitch at $\mathcal{P} = 0$ and (d) coupled motion at $\mathcal{P} = 0$ and $\alpha = 20°$ .Black dots: BvK street. Grey dots: reversed BvK wake. White dots: wake symmetry breaking. The dashed black curves correspond to the best fit curves of the neutral line.

is suitable to examine a specific kinematics, it is clear that this does not universally describe wake transitions. This is the result of the unique interactions between LEVs and TEVs that are specific to the motion type. Consequently this demonstrates the need for a self similar classification of the oscillating amplitude to accurately determine wake development.

4.2.2 An Alternative Length Scale

Fundamentally, the foil generates thrust force by displacing and accelerating fluid out of its path as it moves through its prescribed trajectory. The quantity of fluid displaced is dependent on the product of the chord length $\mathcal{C}$ times the path length travelled by the foil over one period of oscillation. Thus,a proper indicator of the wake's drag-to-thrust transition should reflect the length of the curve traversed by the foil within a cycle.

To quantify the aforementioned distance, we compare different length approximations of the path length ($\mathcal{L}$) covered by the TE in one non-dimensional period for a heaving foil. We estimate this length in three different ways:(a) step motion,(b) square wave and (c) sine wave. As shown in figure 4.6a (red curve) the step motion definition is equivalent

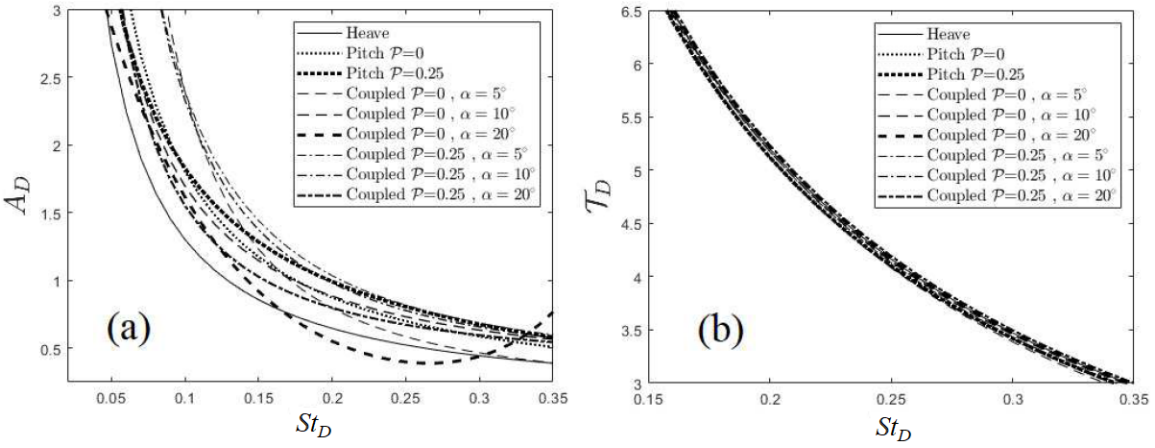

Figure 4.5: Comparison of neutral line best fit curves for various kinematics on a $St_D - A_D$ phase space (a) and a $St_D - \mathcal{T}_D$ phase space (b) at $Re = 1173$. Here $\mathcal{T}_D$ is the thickness normalised $\mathcal{T}$.

to the use of A to capture the covered length. As we see in figure 4.6b the square wave length Sq captures A in the vertical direction but also the streamwise length (U_∞/f) traversed by TE in one period. Finally the *trajectory* length Tr of the sine wave (see figure 4.6c) captures the exact $\mathcal{L}$ traversed by the TE over the entire period:

$$T_r = U_\infty \int_0^{1/f} \sqrt{\dot{x}^2(1,t) + \dot{y}^2(1,t)}dt, \tag{4.1}$$

where $\dot{x}$ is the horizontal velocity of the foil, which is approximately U_∞ for small amplitude motions.

The utility of these three metrics is estimated via the agreement (collapse) of the neutral curves for different types of motions in the $f - \mathcal{L}$ domain. Here the $\mathcal{L}$ is normalised by D and this is done so that f can be expressed by St_D at the same domain. Again figures 4.6a, 4.6b and 4.6c show the neutral lines for different kinematics in $\mathcal{L}_D - 1/St_D$ domains for the aforementioned types of $\mathcal{L}_D$ namely: A_D, Sq_D and Tr_D respectively. The frequency is represented in the inverse form so that a power law between amplitude and frequency is depicted by a straight line. Since previous studies suggest that BvK reversal depends solely on St_A, we expect a collapse of the neutral line curves of different kinematics when plotted on an $A_D - 1/St_D$ chart. However as seen in figure 4.6a these curves are heavily dependent on kinematics. On the other hand, as we move towards Tr (which accurately represents the trajectory length) the collapse of the various neutral line curves is significantly improved (see figure 4.6c).

Tr is suitable for characterising heave dominant kinematics since the motion of the entire chord can be represented just by the path traversed by the TE. This means that the displaced fluid per cycle of a heave dominant motion can be expressed as $Tr \cdot \mathcal{C}$.

However, Tr fails to capture the effects of a chordwise gradient A present in pitch-dominated motions since most of the lateral motion is downstream of the pivot point for $\mathcal{P} < 0.5$ (see figure 4.3b). This means that Tr overestimates the displaced fluid for these particular cases and therefore it is still dependent on kinematics (see figure 4.6c). The effect of the pitching component can be incorporated into the metric by calculating the *average* trajectory length covered by the entire foil (chord) over one period:

$$\mathcal{T} = \tilde{\mathcal{L}} = U_\infty \int_0^1 \int_0^{1/f} \sqrt{\dot{x}^2(t,s) + \dot{y}^2(t,s)}\; dt\; ds \tag{4.2}$$

where, s is the coordinate along the chord with $s = 0$ at LE and $s = 1$ at the TE.

The D-normalised chord averaged trajectory length $\mathcal{T}_D$ is plotted versus $1/St_D$ in figure 4.6d. The new metric demonstrates remarkable collapse of different kinematics on the curve corresponding to the neutral line of pure heave (where $Tr_D = \mathcal{T}_D$). Interestingly this curve roughly follows the diagonal of a square which can be expressed as $\mathcal{T}_D \cdot St_D \sim const = 1$. This product represents the average speed of the foil over one period. Thus the area in the lower right half of the straight line represents the zone where this average speed is less than U_∞ while the the upper left is where the speed is larger than U_∞. This provides a very simple physical interpretation of the $1/f - \mathcal{T}$ phase space where, in order for the foil to produce thrust, the kinematics has to be tuned in such a way that the chord averaged speed of the foil along the path over one period must be faster than the free stream. In other words, a path length based Strouhal number ($St_\mathcal{T} = f\mathcal{T}/U_\infty$) should be greater than 1. As the value of $St_\mathcal{T}$ increases further beyond 1, the wake of the foil becomes stronger producing higher and higher values of thrust.

The universality of the new length scale is evaluated by further examining the agreement of neutral line curves for various kinematic factors such as f, $\mathcal{P}$, α. Figure 4.5b shows all the kinematic options where a collapse was demonstrated. The agreement among these curves deteriorates for $St_D < 0.12$ or $St_D > 0.35$ perhaps due to the limitations of using two dimensional numerical simulations. This is consistent with the observations of Mittal and Balachandar (1995) who found that 2D simulations might result in large force fluctuations and erroneous wake patterns. Additionally non periodic wakes have been observed for pure pitch motion at $\mathcal{P} > 0.6$ which could also contribute to the poor collapse. As α is essentially an indicator of the heave to the pitch ratio within a coupled motion case it has no real effect on periodicity at least up to $\alpha = 20°$ and thus the coupled motions presented here agree well with the pure pitch and heave test cases. Clearly the new metric sets a threshold for the drag-to-thrust wake transition of 2D flapping foils for the entire range of kinematics provided that the resultant wake is periodic.

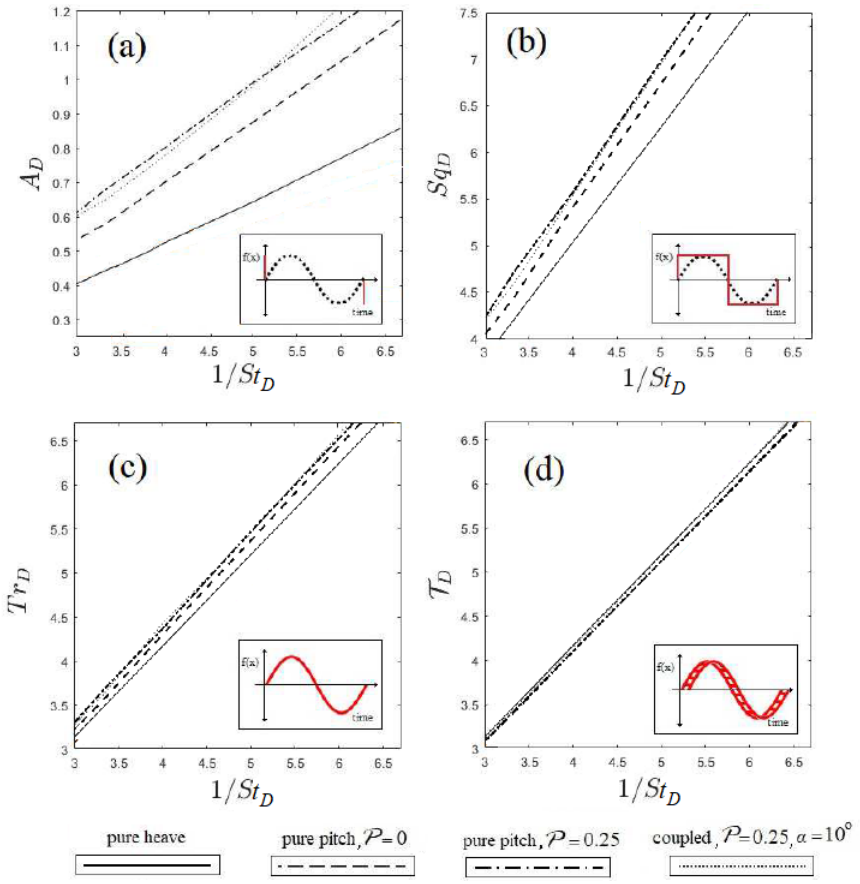

Figure 4.6: Best fit curves of the neutral line of various harmonic kinematics plotted on $A_D - 1/St_D$ (a) , $Sq_D - 1/St_D$ (b) , $Tr_D - 1/St_D$ (c) and $\mathcal{T}_D - 1/St_D$ (d). Each point on the y-axis expresses the thickness normalised length of the curve (red) of the corresponding approximation of the path traversed by the foil within one cycle.

4.2.3 Validation to non-sinusoidal kinematics of a wedge type foil

Having verified the utility (and limitations) of our scaling method for harmonic kinematics we proceed with the analysis of non-sinusoidal motions. More specifically, we focus on the data derived from Chao et al. (2019a) regarding a wedge type foil with semi circular LE (Godoy-Diana et al., 2008b) undergoing pure pitch at the same $Re_{\mathcal{C}} = 1173$. Here the thickness is given non dimensionally as $\mathcal{C}/D = 5/23$ while the pivot point is defined as $\mathcal{P} = D/2$. Moreover, the non sinusoidal nature of the motion is imposed through a function of $\theta(t)$ derived by (Lu et al., 2013):

$$\theta(t) = \frac{\theta_0 \arcsin[-K \sin(2\pi f)]}{\arcsin(-K)}, \quad -1 \leq K < 0$$

$$\theta(t) = \sin(2\pi f), \quad K = 0 \tag{4.3}$$

$$\theta(t) = \frac{\theta_0 \tanh[K \sin(2\pi f)]}{\tanh(K)}, \quad K > 0$$

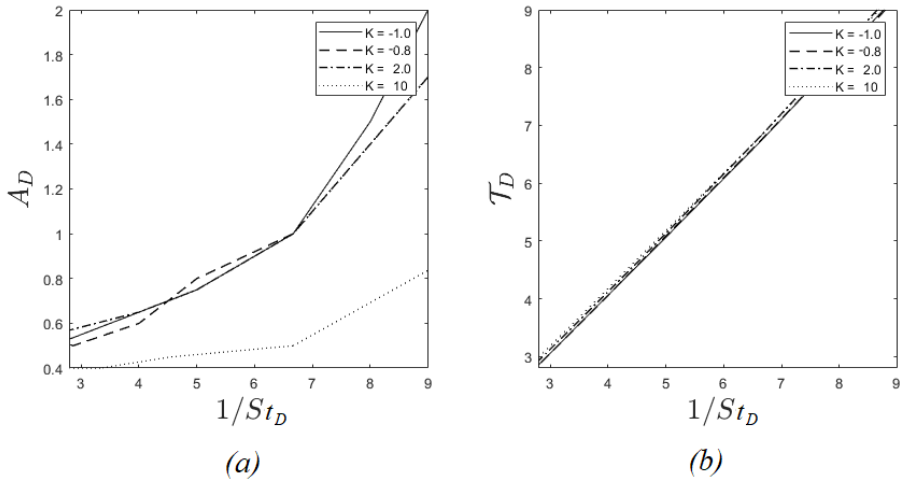

Figure 4.7: Drag to thrust wake transition for non sinusoidal pure pitching foils in (a) $A_D - 1/St_D$ and (b) $\mathcal{T}_D - 1/St_D$ plots.

where the parameter K is adjusted accordingly so that the kinematics vary from a saw-tooth wave at $K = 1$ to a square wave at $K \sim \infty$.

Figure 4.7 shows the location of the neutral line patterns of the four non sinusoidal cases studied by (Chao et al., 2019a) in plots of $A_D - 1/St_D$ as well as $\mathcal{T}_D - 1/St_D$ where A_D and $\mathcal{T}_D$ denote the thickness normalised TE amplitude and $\mathcal{T}$ respectively. Clearly there is a good agreement among $\mathcal{T}_D$ as all four motions collapse upon a linear curve at a 45^o slope in a similar manner to the harmonic motions studied previously. This is due to the fact that $St_{\mathcal{T}}$ expresses the required displaced volume over a cycle in order to achieve propulsion. Thus, it is independent of the instantaneous kinematics and/or the profile shape of the moving body.

4.2.4 Effects of profile thickness

To investigate the effects of the profile thickness we conduct pure heaving simulations at $Re = 1173$ for symmetric NACA00XX profiles where $D \sim [0.075 - 0.2]\mathcal{C}$. As seen in figure 4.8 $\mathcal{T}_D$ shows a better curve collapse than A_D with minor discrepancies observed in the range $D \sim [0.12 - 0.18] \cdot \mathcal{C}$. However, both thicker and thinner foils present a non linear behaviour,so that no single $St_{\mathcal{T}}$ threshold can be found for the investigated wake transition.

A varying thickness has been observed to alter the flow field around the foil and thus the resulting wake. More specifically, the sharp LE of very thin profiles tend to generate large LE separation bubbles as opposed to the medium thickness profiles (see figure 4.9 a). A wider separation bubble means less positive dp/dx available downstream and therefore smaller overall ΔP. In addition, this ΔP is applied on the comparatively smaller frontal area of the thinner foil which eventually leads to less generated thrust (Lentink and

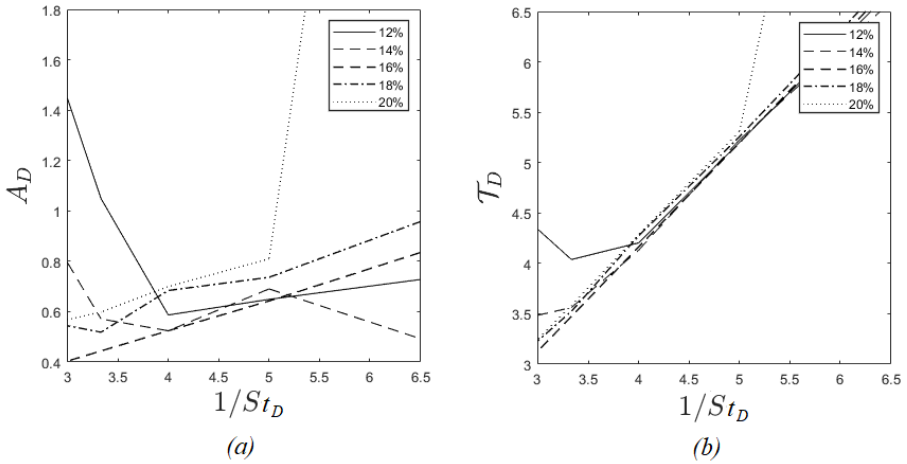

Figure 4.8: Drag to thrust wake transition of pure heaving foils of varying thickness in (a) $A_D - 1/St_D$ and (b) $\mathcal{T}_D - 1/St_D$ plots.

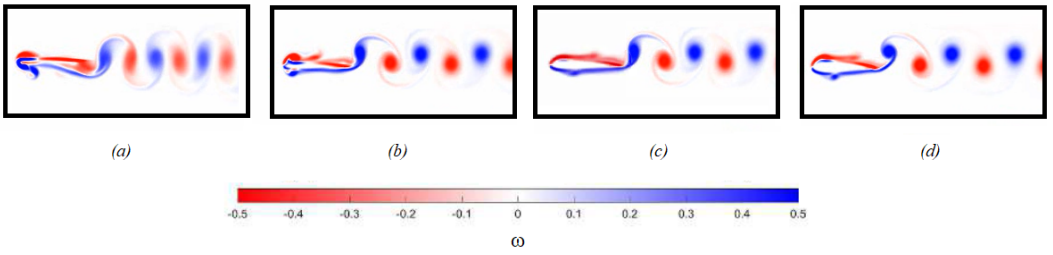

Figure 4.9: Normalised vorticity field at $Re = 1173$ for symmetric foils of (a) $D = 0.075\mathcal{C}$ (b) $D = 0.125\mathcal{C}$ (c) $D = 0.16\mathcal{C}$ and (d) $D = 0.2\mathcal{C}$ undergoing pure heave. Note that all test cases perform for the same $\mathcal{T}_D$.

Gerritsma, 2003; Ashraf et al., 2011). On the other hand, when $\mathcal{D}$ is significantly large, LE vortices are generated downstream of the maximum thickness point (see figure 4.9 d) which reduces the distance available for the development of a positive ΔP.

The aforementioned phenomena can explain the changes in the ambient flow which in turn affect the propulsive capacity of the oscillating body. However, as the definition of $\mathcal{T}$ is purely based on the kinematic input (and the corresponding fluid displacement), it is not expected to be influenced by the foil´s thickness. This paradox can be attributed to the limitations of the two dimensional field as discussed in previous sections. The hypothesis of erroneous wake patterns is at least possible for the very thin foils where the large LEV´s are comparable in size and strength to the ones formed by the NACA0016 outside of the St_D range where $\mathcal{T}$ is considered reliable. Yet, a verification of this theory requires an extensive three dimensional analysis which is well beyond the scope of this study.

4.3 Conclusions

Two dimensional simulations were conducted for a rigid flapping NACA0016 profile at $Re_{\mathcal{C}} = 1173$. The wake development towards a reversed BvK street was examined for a variety of harmonic motions, amplitudes and frequencies. At very low amplitudes and frequencies 2P wake patterns were observed for the coupled motions in agreement with either the pure heave or the pure pitch cases. This is due to the fact that at such low $St_D - A_D$ combinations the coupled motions are dominated by either the heaving or the pitching component.

In dimensionless Amplitude-Period maps various length scales were evaluated with respect to the neutral line of different motion types. It was revealed that the relationship between A_D and the period is non-linear since the maximum distance from equilibrium cannot properly characterise the displaced volume (or area) required to overcome the drag forces. This is solved by calculating the length of the path traversed by the foil over one period of oscillation.

On a $1/St_D - Tr_D$ graph the neutral line of pure heave forms a linear curve $y(x)$ where $dy/dx = 45°$. Since $U_{foil} = Tr_D/(1/St_D)$ this means that thrust is achieved when $U_{foil} > U_\infty$. Furthermore the dimensionless chord average trajectories per cycle $\mathcal{T}_D$ of all motion types tested, collapse upon the pure heaving case. In other words the neutral lines of all test cases collapse on a trajectory-based Strouhal $St_{\mathcal{T}} \to 1$. This was also verified for non-sinusoidal motions derived from published data. Thus the new metric can serve as an adequate length scale that captures the BvK reversal for every combination of two dimensional kinematics.

The universality of $\mathcal{T}$ is challenged by a variety of geometric and kinematic factors. More specifically, it is found that a good agreement exists only when: $\mathcal{P} < 0.6$, $0.12 < St_D < 0.35$ and $0.12\mathcal{C} < D < 0.2\mathcal{C}$. It is suggested that these limitations are related to the limitations of the 2D solver, although more research in the field is required.

In conclusion, this novel method allows us to parametrise drag-to-thrust wake transition of a simple two dimensional oscillating body via the chosen kinematics without the use of complex fluid dynamic equations. Knowing the onset of thrust for a flapping foil via a single parameter can significantly reduce the effort of designing sufficient biomimetic propulsors. Moreover it will enable scientists and engineers to describe and/or confirm observations regarding the thrust generating strategies and evolution of natural flyers and swimmers.

Chapter 5

Deflected wake interaction of tandem flapping foils

5.1 Overview

Due to their prevalence within the airborne and aquatic wildlife, single flapping foils have caught the interest of scientists and engineers alike since the early twentieth century (Knoller, 1909; Betz, 1912). Moreover, tandem flapping configurations e.g. insect wings (Alexander, 1984; Thomas et al., 2004), plesiosaur flippers (Muscutt et al., 2017a) etc. are shown to outperform single flappers under certain wake-to-wake interactions.

For a single flapping foil the onset of thrust generation is marked by a reverse *von Kármán* street (see figure 5.1b) downstream of its trailing edge (T.E.) (Von Karman, 1935), although a lag between the two conditions exist (Godoy-Diana et al., 2008a; Bohl and Koochesfahani, 2009; Lagopoulos et al., 2019). This wake pattern is determined by the oscillating T.E. amplitude A and frequency f of the motion, which form together an *amplitude based* Strouhal number $St_A = (2fA)/U_\infty$ as described by Triantafyllou et al. (1991). An increasing St_A leads to permanent deflection of the jet (see figure 5.1c) and thus side force generation even when both the camber and the mean angle of attack are zero (Godoy-Diana et al., 2009; Cleaver et al., 2012). This is the result of *dipole* formation when shedding vortices become strong enough to attract each other and depart from the centreline (Godoy-Diana et al., 2009, 2008a). Although three dimensional effects compromise the coherence of these structures (Zurman-Nasution et al., 2020), the formation and subsequent deflection of the dipole maintains its quasi two dimensional nature (Couder and Basdevant, 1986; Godoy-Diana et al., 2008a).

To improve the propulsive performance of a flapping system, various researchers have proposed the use of multiple foil configurations. In particular, tandem flapping foils are shown to improve thrust generation via *wake recapture* both numerically (Muscutt

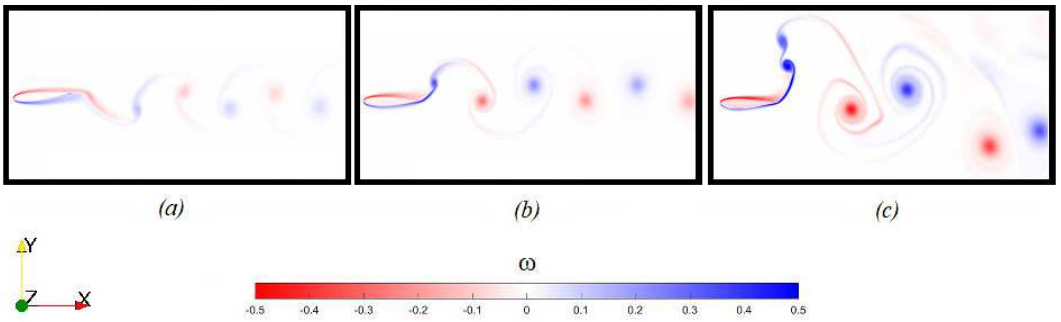

Figure 5.1: Wake transitions of a flapping foil undergoing heave to pitch coupling at $St_C = 0.625$: (a) *von Kármán* street at $A_C = 0.2$ (b) reversed *von Kármán* street at $A_C = 0.3$ and (c) deflected jet at $A_C = 0.4$.

et al., 2017b; Broering and Lian, 2012c; Akhtar et al., 2007) and experimentally (Muscutt et al., 2017a; Warkentin and DeLaurier, 2007; Usherwood and Lehmann, 2008b). More specifically, thrust and efficiency augmentation can be achieved when the hind foil is weaving within the incoming vortices shed by the front one, determined by the inter foil spacing and phase lag.

A prominent feature of these studies is the relative lack of influence the downstream foil is said to have on the wake and forces of the upstream foil. However, those studies focus on cases with symmetric reverse *von Kármán* streets where momentum exchange between shedding vortices is minimal. On the other hand, vortices of deflected wakes are often in very close proximity to each other, forming a long chain of well defined and correlated dipoles.

This paper focuses on the interaction between deflected wakes of tandem flapping foils undergoing harmonic motion. Simulations are conducted for single and tandem flapping configurations at a range of St_A that ensures steady dipole formation. As the primary mechanism for wake deflection is two dimensional, we restrict ourselves to two-dimensional simulations in this work. It is revealed that certain phase-spacing combinations neutralise deflection for both foils. Distinct types of wake to wake interaction are observed and described in terms of their propulsive characteristics. In addition we clarify the mechanism of deflection cancellation and determine its limits in terms of a simple non-dimensional parameter, the spacing based Strouhal number.

5.2 Methodology

Figure 5.2 shows the basic elements of the simulated configuration. Two rigid NACA0016 with a thickness $D = 0.16\ \mathcal{C}$ (where $\mathcal{C}$ is the chord length) undergo sinusoidal heave to pitch coupling at $\mathcal{P} = 0.25$, against a uniform free stream velocity U_∞ for a $\psi = 90°$.

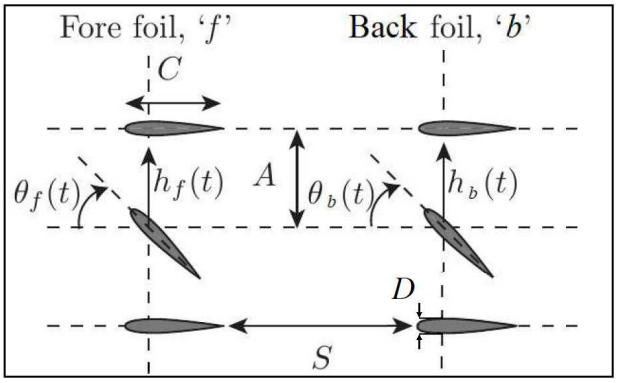

Figure 5.2: The kinematic parameters of a tandem configuration. Redrawn from Muscutt et al. (2017b).

In a similar fashion to Chapter 4 various frequencies and TE amplitudes are tested but in terms of $St_{\mathcal{C}}$ and A_C as the $\mathcal{C}$ is deemed as a more adequate length scale for the purpose of this study. In addition all simulations of the section are performed at a Reynolds number of $Re_{\mathcal{C}} = 1173$ to allow comparison with published work in the field (Godoy-Diana et al., 2009, 2008a; Andersen et al., 2017; Chao et al., 2019b).

Wake deflection is analysed both qualitatively (visualisation) and quantitatively through the generated side forces. These are expressed via the $\widetilde{C}_l, i$ which can refer to the single, front or back foil described by their respective subscripts s, f, b. Likewise, thrust generation is expressed via $\widetilde{C}_t, i$.

5.3 Results and discussion

5.3.1 Single foil analysis

Single foil arrangements undergoing harmonic heave to pitch coupling are tested for $St_C \sim [0.625\ ,\ 2.5]$ and $Re = 1173$ in a two dimensional domain. A_C is chosen so that $\widetilde{C}_{l,s} \sim 0.4 = const.$ across the entire St_C range. The kinematic details and resulting $\widetilde{C}_{l,s}$ are shown in table 5.1.

The resultant wakes (see figure 5.3) maintain the basic features and deflection mechanism of asymmetric jets reported in literature for pure pitch (Godoy-Diana et al., 2009, 2008a; He et al., 2012) and pure heave (Cleaver et al., 2012; Kozłowski and Kudela, 2014). Vortex circulation Γ is proportional to the flapping frequency while the opposite is true for the distance between consecutive vortices. In the beginning, the first shed vortex follows an independent path away from the centreline. Yet, the distance between the second and the third subsequent vortices is noticeably smaller. This results in the formation of a dipole as shorter distances lead to stronger synergy among vortices according to the $Biot - Savart$ vortex induction law (Zheng and Wei, 2012). The initial

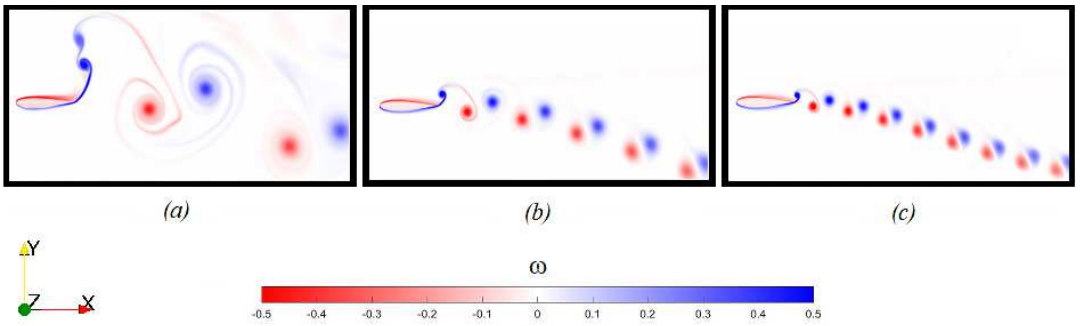

Figure 5.3: Normalised vorticity field of a single flapping foil undergoing harmonic heave to pitch coupling at (a) $St_C = 0.625$, (b) $St_C = 1.5625$ and (c) $St_C = 2.5$. All produced wakes are steadily deflected generating $\widetilde{C}_{l,s} \sim 0.4$.

St_C	A_C	$\widetilde{C}_{t,s}$	$\widetilde{C}_{l,s}$
0.6250	1.405	0.59	0.400
0.9375	0.651	0.49	0.400
1.2500	0.437	0.42	0.400
1.5625	0.326	0.37	0.400
1.8750	0.258	0.32	0.390
2.1875	0.213	0.28	0.395
2.5000	0.181	0.33	0.405

Table 5.1: Kinematics and cycle averaged force coefficients of a single flapping foil undergoing heave to pitch coupling for a variety of St_C, $\alpha = 10°$ and $\psi = 90°$. All cases result in steady wake deflection.

dipole departs from the centerline, breaking the symmetry of the mean jet and imposing its path to the subsequent dipole (Godoy-Diana et al., 2008a).

5.3.2 Tandem foil analysis

Two dimensional tandem foils are tested for the kinematics and Re of the previous section. Simulations are performed for a wide range of spacings $\mathcal{S}_C \sim [1-6]$ and $\varphi \sim [0-1.75]\pi$ in increments of $\pi/8$, respectively. It is revealed that, at certain $\mathcal{S}_C$ - φ combinations, the presence of the downstream foil results in a stable symmetric wake and zero net lift, even for the upstream foil. Specifically, we define lift cancellation as the condition when:

$$|\widetilde{C_{l,f}}| < \epsilon \quad , \quad |\widetilde{C_{l,b}}| < \epsilon \quad , \quad |\widetilde{C_{l,f}} + \widetilde{C_{l,b}}| < \epsilon$$
$$where \qquad \epsilon = 0.05\ \widetilde{C_{l,s}} \tag{5.1}$$

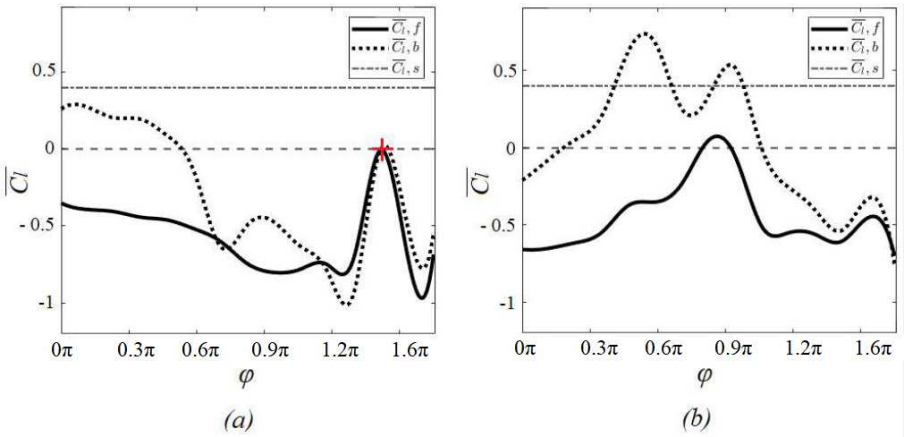

Figure 5.4: Cycle averaged Lift coefficient versus phase for a tandem foil configuration at $St_C = 1.25$ and (a) $\mathcal{S}_C = 3$, (b) $\mathcal{S}_C = 4$. The red cross in plot (a) marks lift cancellation.

This condition is illustrated for two spacing at $St_C = 1.25$ in figure 5.4. At $\mathcal{S}_C = 3$ and $\varphi = 1.5\pi$ both $\widetilde{C}_l$ curves are converging to zero, demonstrating complete lift cancellation on the front and back foil due to wake interaction. However, at $\mathcal{S}_C = 4$, while at least two phases lead to $\widetilde{C}_{l,f} = 0$, there is no phase which causes lift cancellation on both foils.

The manner in which the lift is cancelled depends on the interaction between the back foil and the incoming wake of the front foil. The specific type of interaction affects both the front and the back wake and has a crucial effect on the system‘s overall thrust (see table 5.2). In figure 5.5, three possible modes of lift cancellation are reported:

- Type I, where the back foil slides within the channel between the two vortices that form the incoming dipole (see figure 5.5a).
- Type II, where the back foil collides with one of the two vortical components of the dipole (see figure 5.5b).
- Type III, which is effectively an intermediate condition between the previous two modes as the aft foil partly collides with the outer region of the incoming vortex (see figure 5.5c).

Interestingly, figure 5.5a shows that at $St_C = 0.625$ lift cancellation is still present even for a $\mathcal{S}_C \sim 5$. In contrast, most published work supports the idea that downstream flow has no impact on the propulsive characteristics of the fore foil. These studies, however, focus on the interaction between non deflected jets where momentum exchange among subsequent vortices and the ambient fluid is minimal.

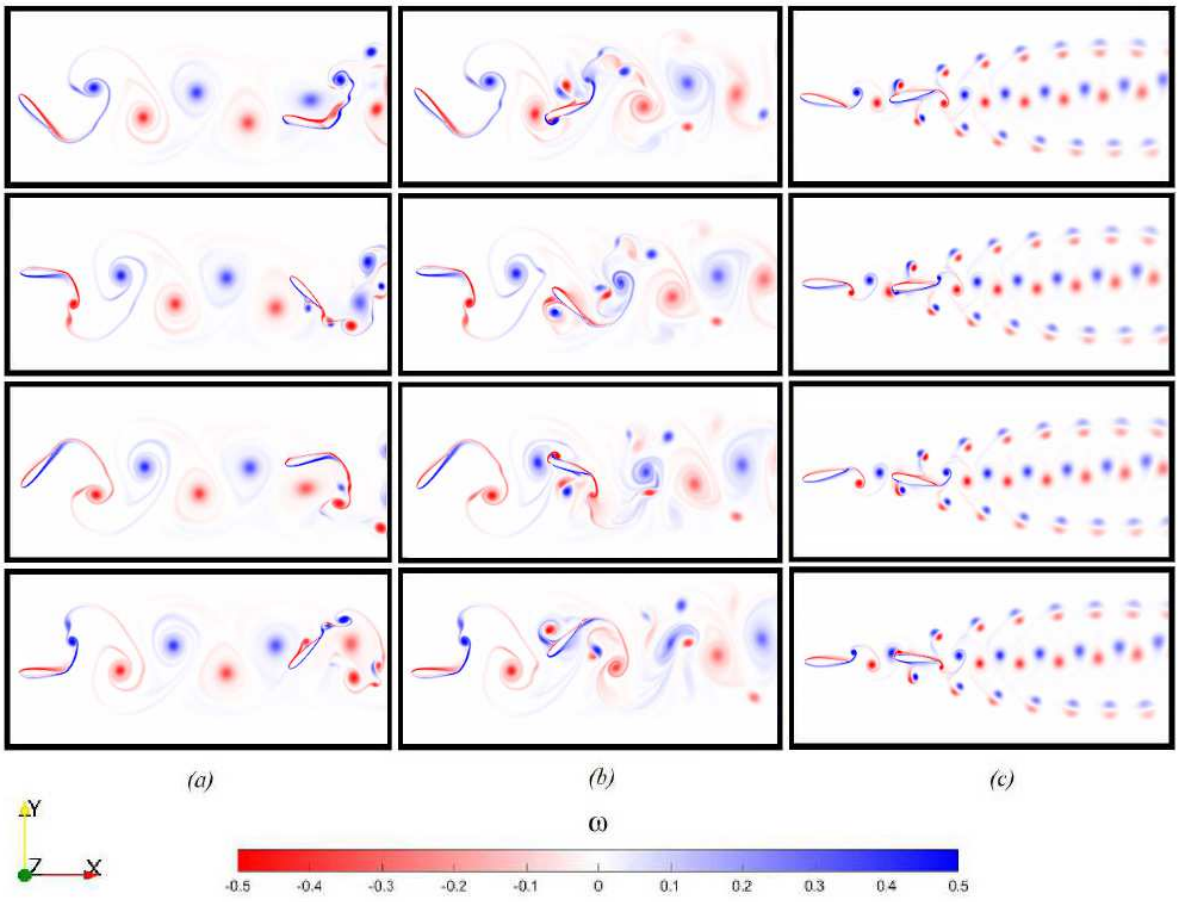

Figure 5.5: Snapshots of normalised vorticity for lift cancelling tandem configurations at cycle increments of $t/T = 1/4$ where $T = 1/f$. Three distinct wake patterns can be observed: (a) Type I at $St_C = 0.625$, $\mathcal{S}_C = 5$ and $\varphi = 1.6\pi$, (b) Type II at $St_C = 0.625$, $\mathcal{S}_C = 2$ and $\varphi = 1.375\pi$ and (c) Type III at $St_C = 1.5625$, $\mathcal{S}_C = 1$ and $\varphi = 0.875\pi$.

Test Case	St_C	A_C	$\mathcal{S}_C$	φ	$\widetilde{C}_{t,f}$	$\widetilde{C}_{t,b}$	$\widetilde{C}_{l,sf}$	$\widetilde{C}_{l,b}$
Single Foil (Symmetric)	0.2000	2.467	-	-	0.535	-	0.000	-
Single Foil (Deflected)	0.6250	1.405	-	-	0.590	-	0.400	-
Tandem Foils (Classic)	0.2000	2.467	5.0	0.500π	0.535	0.910	0.002	0.014
Tandem Foils (Type I)	0.6250	1.405	5.0	1.600π	0.969	3.076	-0.019	0.022
Tandem Foils (Classic)	0.2000	2.467	2.0	1.500π	0.535	0.909	-0.017	0.033
Tandem Foils (Type II)	0.6250	1.405	2.0	1.375π	0.646	-1.191	0.039	-0.013
Tandem Foils (Classic)	0.2000	2.467	1.0	0.000π	0.535	0.828	-0.003	0.010
Tandem Foils (Type III)	1.5625	0.326	1.0	0.875π	0.595	0.340	0.030	0.002

Table 5.2: Mean force coefficients $\widetilde{C}_t$ and $\widetilde{C}_l$ of single and tandem flapping foils for kinematics resulting in symmetric and deflected wakes. Tandem combinations of non deflected wakes are referred to as *classic*.

5.3.3 Thrust considerations

Thrust augmentation is a well reported phenomenon of in line flappers. When the back foil weaves between the incoming vortices, it experiences a higher U_∞ compared to the front foil. This increases its thrust generation capacity and cases of $\widetilde{C}_{t,b} \sim 2\widetilde{C}_{t,f}$ have been observed (Muscutt et al., 2017b). Table 5.2 shows that Type I wake modes manage to exceed these values reaching up to $\widetilde{C}_{t,b} \sim 2.7\widetilde{C}_{t,f}$. This should be expected since Type I occurs at a much higher St_C compared to symmetric wake cases found in literature. Hence the circulation of the wake vortices experienced by the back foil is greater enabling the formation of similarly increased strength vortices by the foil and thereby a higher thrust augmentation.

Figure 5.6 shows the differences in the time averaged streamwise velocity between high performance conventional cases at $St_C = 0, 2$ and Type I modes at $St_C = 0.625$. Conventional test cases utilize the optimal combinations $\varphi = 0\,\pi$, $\mathcal{S}_C = 1$ and $\varphi = 0.5\,\pi$, $\mathcal{S}_C = 5$ derived from the work of Muscutt et al. (2017b) while Type I wake modes are derived for $\varphi = 1\,\pi$, $\mathcal{S}_C = 1$ and $\varphi = 1.6\,\pi$, $\mathcal{S}_C = 5$ respectively. Clearly, the peak value of $\widetilde{u}_x/U_\infty$ is much higher within Type I wakes due to the higher circulation of the vortices. Furthermore, the comparatively shorter distance between these vortices leads to a much narrower jet. Since $T = \int u^2 dy$, this condition enables the higher values of thrust reported above.

5.3.4 The physics of lift cancellation

The mechanism of lift cancellation is depicted in figure 5.7a. The initial dipole shed from the leading foil advects downstream and splits in to two after colliding with the vertically moving aft foil. Consequently, the advection speed of the clockwise vortex (red) decreases which reduces its distance from the subsequent dipole shed by the front foil. This affects the cohesion of the second dipole and its clockwise vortex (blue) is now under the influence of two counter-clockwise vortices. This situation propagates upstream, affecting every subsequent dipole in the same manner, resulting in wake convergence towards the centreline forming a classic reverse *von Kármán* street.

As the collision of the first dipole with the rear foil is necessary for the lift cancellation, we need to examine the circumstances that would lead to this interception. By definition, a collision between two entities is only possible if their paths intersect. Assuming that the first dipole travels along an inclined downstream path set by the initial advection speed (see figure 5.7b), it can be shown that this path diverts from the freestream at an angle of $tan\theta_d \propto fA/U_\infty$ (or $\tan\theta_d = pfA/U_\infty$). This is based on assuming that the horizontal advection speed is proportional to the freestream speed (U_∞) and the vertical advection speed is proportional to the vertical speed of the trailing edge of the front foil (fA). Note that the actual path of the dipole is not a straight line as it follows a more

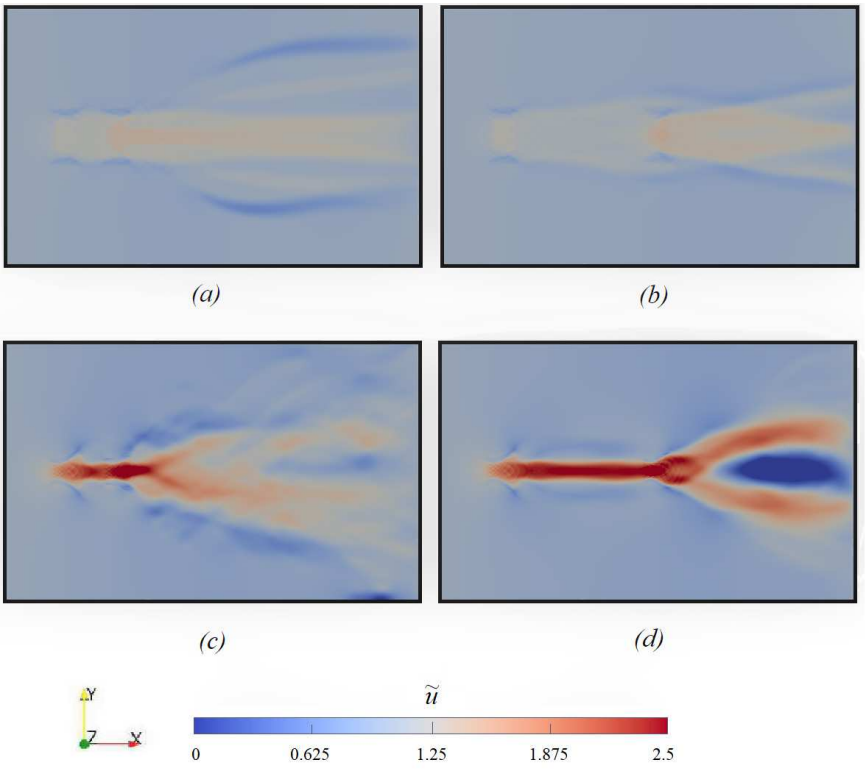

Figure 5.6: Time-averaged streamwise velocity $\tilde{u} = \widetilde{u}_x/U_\infty$ of tandem configurations at $\mathcal{S}_C = 1$ (left column) and $\mathcal{S}_C = 5$ (right column). Patterns at (a) and (b) show results for high thrust enhancement for a non-deflected wake case with $St_C = 0.2$ while (c) and (d) represent type I wake modes with $St_C = 0.625$.

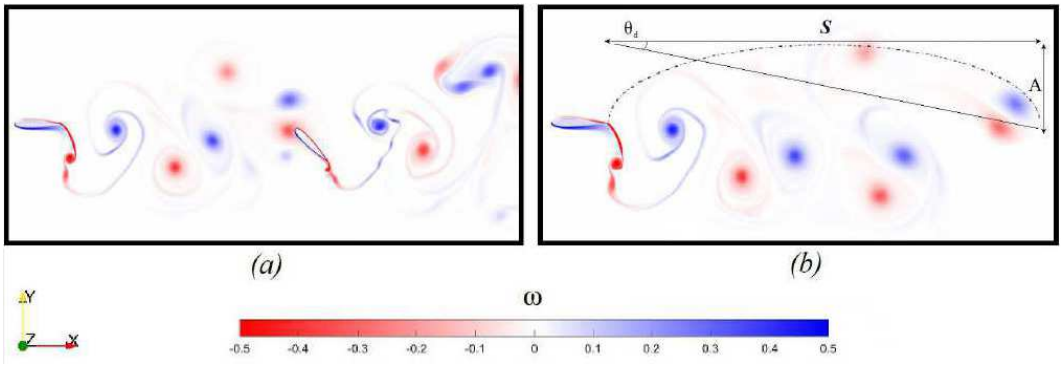

Figure 5.7: Normalised vorticity field of tandem (a) and single (b) foils at $A_C = 1.405$ and $St_C = 0.625$. The initial dipole of a single foil travels in an elliptical path (dashed line) which enhances deflection during its final stages. However, the presence of a downstream flapping foil at an angle $\geq \theta_d$ leads to the decomposition of this first dipole, forcing the incoming jet to maintain symmetry.

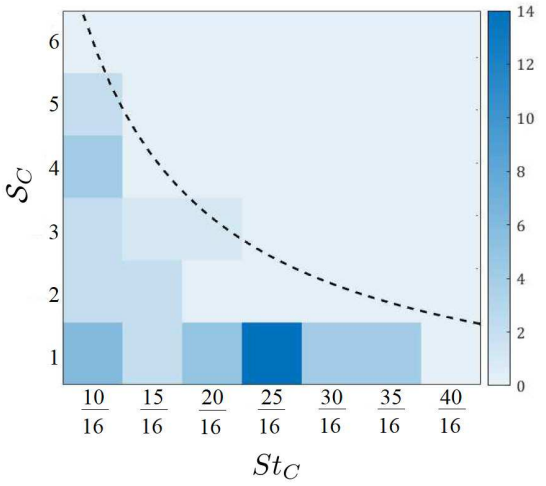

Figure 5.8: Heatmap of lift cancellation instances for a tandem foil system and the full range of $\varphi \sim [0\pi - 1.75\pi]$ and various $St_C - \mathcal{S}_C$ combinations. The dashed curve marks the boundary of possible lift cancellation occurrence and corresponds to a *spacing based* Strouhal $St_{\mathcal{S}} = f\mathcal{S}/U_\infty = 4$.

complex elliptic path. However, the factors leading to the overall angle are sufficient for this discussion. To achieve lift cancellation, this angle, $\tan\theta_d$, must be smaller than the largest angle between the trailing edge of the front foil and the L.E. of the back foil, $\tan\theta_g = A/\mathcal{S}$ so that:

$$\begin{gathered}\tan\theta_d \leq \tan\theta_g \;\rightarrow\; pfA/U_\infty \leq A/\mathcal{S} \\ \therefore f\mathcal{S}/U_\infty \leq 1/p\end{gathered} \tag{5.2}$$

This suggests that there is a *spacing based* Strouhal number that will act as a clear boundary between areas where lift cancellation is possible and areas where wake deflection is maintained. This geometric relationship accounts for all possible phase differences between the fore and aft foils and could even be independent of the frequency of the aft foil. This Strouhal number only depends on the ratio between the horizontal and vertical advection speeds of the dipole shed by the front foil which may vary with the kinematics of the front foil.

The number of lift cancellation instances are plotted on the map of figure 5.8 as a function of non-dimensional spacing ($\mathcal{S}_C$) and non-dimensional frequency ($f\mathcal{C}/U$). We observe that lift cancellation is impossible above a certain region marked with dashed solid black curve. This curve has the form $St_C * \mathcal{S}_C = f\mathcal{S}/U_\infty = const.$. Fitting this equation to the data in figure 5.8 gives a $spacing - based$ Strouhal number that determines the lift cancellation border at $St_{\mathcal{S}} = f\mathcal{S}/U_\infty \sim 4$. Taking into account 5.2 this means that $p = 1/4$. In other words, for a given spacing $\mathcal{S}_\mathcal{C} = 1$ the back foil has the opportunity to impose wake symmetry only if its vertical speed is approximately less than (or equal to) a quarter of the horizontal advection speed of the first shed dipole.

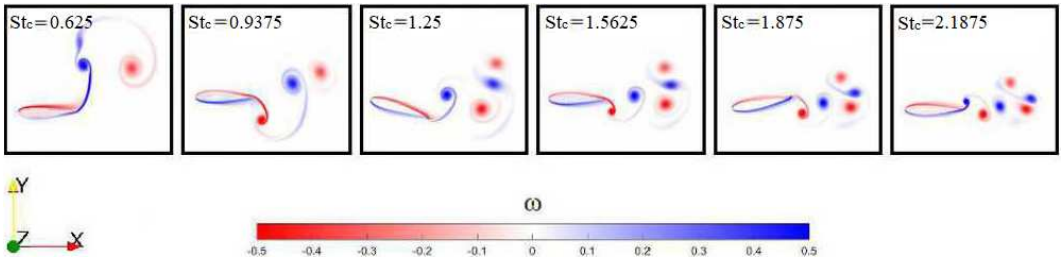

Figure 5.9: Early stages of wake development at $\mathcal{S}_C = 1$ downstream of a single flapping foil.

A careful look at figure 5.8 reveals that the highest concentration of lift cancellations occurs at $\mathcal{S}_C = 1$ and $St_C = 25/16 = 1.5625$. Once again this is linked to the development and propagation of the first permanent dipole. Figure 5.9 shows that at $St_C = 1.5625$ and $\mathcal{S}_C = 1$ the path of the dipole coincides with the centreline. In addition, the channel between its two vortices is approximately equal to the thickness of the back foil. This is an ideal condition, as it maximises the chances of collision with the dipole and thus the number of φ that lead to lift cancellation. Any increase in the St_C changes the direction of the dipole and narrows the channel between its vortices, making it harder to dissolve by the back foil. On the other hand, a lower frequency leads to underdeveloped and more disoriented dipoles, minimizing the chances of impact. Consequently the amount of φ able to eliminate $\widetilde{C}_l$ is reduced and with it, the amount of lift cancellation instances. This essentially describes a Goldilocks condition where the $St_C = 1.5625, \mathcal{S}_C = 1$ is the optimal combination for lift cancellation throughout the tested parameter space.

5.4 Conclusions

Flapping foils, generating fully deflected wakes, are analysed in both single and tandem configurations undergoing coupled heave and pitch kinematics. We find that deflected wakes generated by foils undergoing coupled heave and pitch motion are similar to those reported for pure heave or pure pitch cases. Likewise, the driving mechanism of deflection is the development of dipole structures and their subsequent departure from the centreline.

Tandem configurations are able to reorder deflected jets into symmetric wakes with $\widetilde{C}_{l,f} = \widetilde{C}_{l,b} \sim 0$. Certain φ , $\mathcal{S}_C$, St_C combinations are shown to direct both wakes back to the centreline even for inter foil distances of 5 chord lengths. To achieve lift cancellation the back foil has to dissolve the first shed dipole of the front wake and this is achieved when the angle between the T.E. of the front foil and the L.E. of the back is greater than the dipole's convection angle. This can be expressed via a maximum *spacing based Srouhal*, $St_{\mathcal{S}} = 4$, above which any lift cancellation is impossible. Physically, this $St_{\mathcal{S}}$ limit implies that the back foil must encounter the upstream wake within a few motion cycles for lift cancellation to be possible.

When the total lift of the tandem configuration is cancelled, the wake downstream becomes symmetric. Three wake modes are reported. Type I occurs when the back foil separates the two vortical components of the incoming dipole by weaving between them which leads to a remarkable increase in $\widetilde{C}_t$. Type II mode occurs when the L.E. directly collides on one of the dipole's vortices which introduces a significant drag penalty. In addition, an intermediate mode Type III is reported whose behaviour varies according to the intensity of the vortex-foil collision.

This study is the first to provide evidence of the significant impact of the downstream field to the front foil. Furthermore, it is demonstrated that the wake deflection can be diminished with a subsequent remarkable thrust enhancement. These findings can support the design of high performance biomimetic propulsors, as a simple change of the back foil's phase enables high thrust generation without side force at high frequencies previously considered impossible.

Chapter 6

Experimental Work

6.1 Overview

After the numerical analysis of the 2D single and tandem flapping foils, we proceed with our experimental investigation, where we focus on the three dimensionality of these systems. Here, we attempt to expand the results of a previous project (Muscutt, 2017) towards the development of a bio-inspired UUV with a tandem flapping arrangement. To this end, we limit our attention to single and tandem flapping configurations undergoing sinusoidal heave to pitch coupling at $St_A = 0.4$ and $Re_{\mathcal{C}} = 8500$.

First we conduct an optimization analysis of α_0 for the chosen St_A and $Re_{\mathcal{C}}$ in terms of propulsive efficiency, which is enabled via the experimental investigation of quasi-2D single flapping foils. These are rectangular wings based on an Eppler 837 with a $\mathcal{C} = 0.1\ m$ and a span that roughly covers the test section (see figure 6.1 a). The particular profile shape is chosen due to its resemblance to the cross section of a *Muraenosaurus* specimen that serves as a basis for the bio-inspired project (Muscutt et al., 2017a).

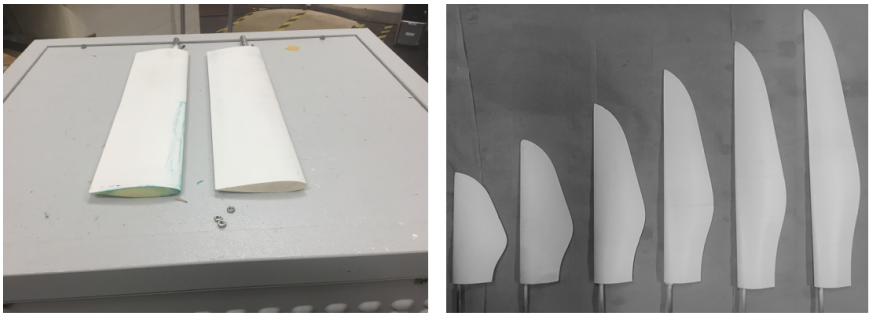

(a) *(b)*

Figure 6.1: (a) Quasi 2D rectangular flippers of an Eppler 837 (left) and a NACA0016 (right) profiles with $\mathcal{C} = 0.1\ m$. (b) Bio-inspired, zero swept flippers of an Eppler E387 with $\tilde{\mathcal{C}} = 0.05\ m$ and increasing AR $\sim [3, 8]$.

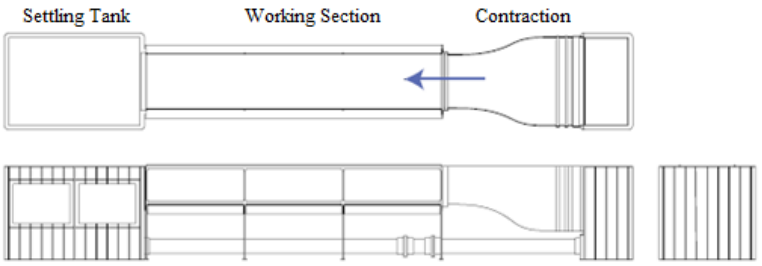

Figure 6.2: CAD model of the flume tank: test section 1.2m x 0.8m and 6.75m long, equipped with two 2-axis pitch-plunge mechanisms for use in flapping wing experiments (Muscutt et al., 2017a).

When the appropriate α_0 is chosen we proceed with the investigation of the bio-inspired configuration, by comparing the behaviour of single and tandem flipper arrangements for increasing aspect ratio. More specifically, the experiments are conducted for the aforementioned St_A and Re at a fixed $\mathcal{S}_C = 2$ and a wide range of AR $\sim$ [3,8] (see figure 6.1 b). These flippers are constructed for the same Eppler 837 with a $\tilde{\mathcal{C}} = 0.05\ m$ and a spanwise geometry which is based on the Collard plesiosaur from the Lower Liassic Kilve shales of Somerset (Muscutt et al., 2017a).

In the following segments we outline the experimental facilities and procedure in detail. Furthermore we explain our calibration procedure and resultant matrices. Lastly, we present our experimental analysis and conclusions.

6.2 Facilities and Equipment

6.2.1 Flume Tank

All experiments are performed in the recirculating flume tank of the department of Aerodynamics and Flight Mechanics (AFM), University of Southampton, UK. General characteristics can be seen in figure 6.2. Flow velocity is determined by a system of two propellers in parallel configuration, driven by two 3-phase motors with $P_{motor} = 17.5Kw$, reaching an upper flow velocity of $U_\infty = 0.8m/s$. Freestream turbulence is limited by a smooth decrease of the cross section, and a honeycomb mesh located before the contraction. The main test section is built by a thin metallic frame and large transparent glass surfaces to enable visualization.

6.2.2 Apparatus

Kinematics and proper placement of the foils are enabled by two robotic arms supported by a towing carriage above the flume tank (see figure 6.3). The frame is made by industrial aluminium profiles. The entire setup rests on two, ten meter long metallic rails,

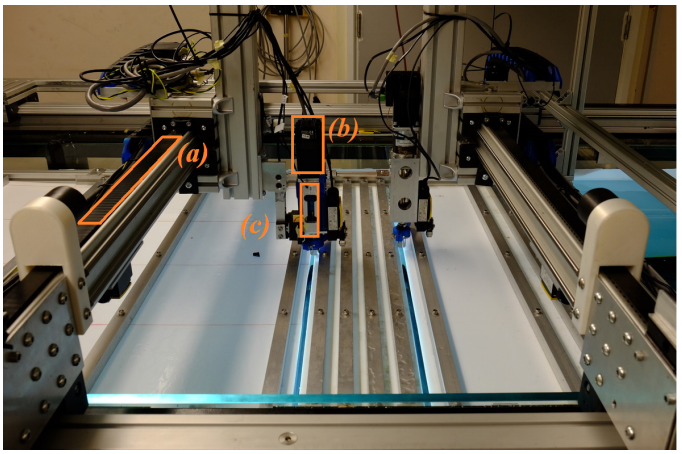

Figure 6.3: Upper view of the carriage system. Heaving motion is enabled by a tracking belt (a) connected to each probe while pitching is generated by a motor on top of the bearing blocks (b). Force measurements are enabled for the back probe via three load cells placed around the root of the flipper (c).

placed upon the sides of the water tank parallel to the freestream. To ensure adequate space for surge motion and easy assembly the rails cover the whole test section. In addition, the frames enable the user to place flat plates parallel to the flow at the height of interest in order to simulate the fuselage of the test object and avoid surface-flipper interaction.

The recent upgrade of the setup expanded its capabilities so that surge is also enabled together with the classic heave and pitch motion. Span-wise motion (heave) is enabled by tracks connecting the probes to motors on the side of the tank. In a similar fashion surge in enabled through a thread of tracks parallel to the freestream and a motor placed at the end of the flume. Finally, the pitching motion is determined by motors on top of the flippers. We should note that steady state experiments can also be performed by fixing the arms to the position of interest.

The hydrodynamic forces and moments are recorded for the aft probe which is equipped with three strain gauges (see figure 6.4). Thus, propulsive differences between the tandem and single arrangements can be traced via the direct comparison of the single and the back foil. To protect flippers and probes from hitting the tank's walls we placed motion sensors at the desired boundaries of the test section. Activation of the sensors leads to immediate stop of the system and repetition of the experiment requires reallocation of the probes and system reboot.

6.2.3 Control System

A compact RIO system equipped with a real-time processor and user-programmable FPGAs serves as the kinematics control system and the signal acquisition device. Thus, the experimental setup performs reliably and sufficiently fast. The main hardware consists

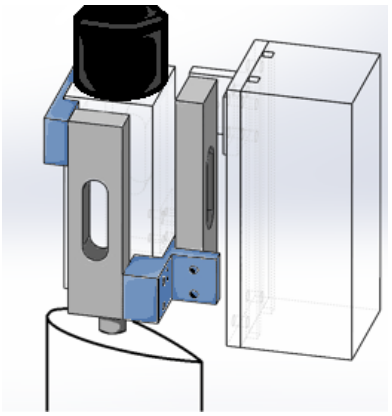

Figure 6.4: Skematic of the aft foil's probe. The flipper is set in motion by the step motor (black), while measurements are taken through the three load cells (grey) attached to special protrusions (blue) of the bearing block.

of a chassis (with the RT-processor) and various analog and digital I/O modules that control either one of the motors or enable data acquisition. The software used to enable the above functions is LABVIEW, a system-design platform and development environment for a visual programming language developed by National Instruments technical advisors (2014). Here it should be noted that recent updates on the LABVIEW script enable modification of the scan engine time as well as the data acquisition time. This further enables the use of different flapping frequencies which is paramount for our thrust augmentation study as seen in Chapter 3.

6.3 Experimental Methods

6.3.1 Load acquisition techniques

As mentioned previously, hydrodynamic loads are measured indirectly by the three strain gauges placed on the aft probe. A data acquisition tool samples instantaneous voltage points from the strain gauge at a frequency $\mathcal{F} = 250\ Hz$, presenting the response of the load cell per oscillating instance. To ensure repeatability all experiments are conducted for 100 flapping cycles where the first and the last 5 are subtracted to account for inertial effects due to the initiation and the finishing process of the motion. The data is then cleared from white noise via the subtraction of a zero motion test case. In addition, random electro-mechanical noise is reduced by special filters (Carlton, 1994), which are set to remove all frequencies larger than 10 times the flapping frequency.

6.3.2 Calibration Process

To assess the propulsive performance of the system, voltage data is converted to force and moment loads via a calibration matrix that was generated prior to the experiments

	F_X	F_Y	M_Z
AI1	84.4	14324.3	192.67
AI2	-3439.27	-35.48	-643.64
AI3	-3407.27	-97.72	661.76
AI1 AI1	-202148.21	1054566.91	211645.91
AI1 AI2	-22103.58	264690.97	106108.95
AI1 AI3	119933.77	238923.95	101051.53
AI2 AI2	-1636359.66	-17167048.33	-1722639.90
AI2 AI3	-2483406.23	-16583188.31	-1678432.67
AI3 AI3	-82395.35	-325282.07	-104819.23

Table 6.1: Second order calibration matrix. Each element describes the relationship between the voltage signal of a strain gauge (left) and the hydrodynamic load that generated it (top).

(see table 6.1). This was achieved by performing empty tank measurements with known weights of increasing value. The resultant matrix contains the multiplication factors that describe the influence of each load cell on the loads, and has units of mV/kg.

Non linear interaction between the loads and the voltage output can lead to serious discrepancies between the measured and the actual signal (de Kat, 2016c,a). To tackle this issue it is common to follow higher order calibration procedures where the correlation among the force vectors of the same sensor is taken into account as seen in the equation bellow:

$$F_i = \sum_{j=1}^{3} A_{ij} S_j + \sum_{j=1}^{3} \sum_{k=1}^{3} B_{ijk} S_j S_k \tag{6.1}$$

where F_i is the physical load of interest, $A_{i,j}$ is the first order factor multiplied by a voltage signal S_j and B_{ijk} is the second order factor multiplied by the product of two voltage signals.

6.3.3 Uncertainty analysis

Since the kinematic parameters of the probes e.g. f, h_0, θ_0 etc. are set to be constant, the cycle averaged loads are not expected to vary per period. It is therefore safe to assume that any discrepancy is the result of a random malfunction. Such uncertainties, related to thrust ($\mathcal{E}_T$) and power ($\mathcal{E}_P$), are taken into account via the standard deviation of the mean:

$$\mathcal{E} = \sqrt{\frac{\Sigma(x_i - \tilde{x})^2}{N}} \tag{6.2}$$

where x_i is the value of interest at each cycle, $\tilde{x}$ is the cycle averaged value and N is the number of flapping cycles. Consequently, errors of the efficiency are estimated by

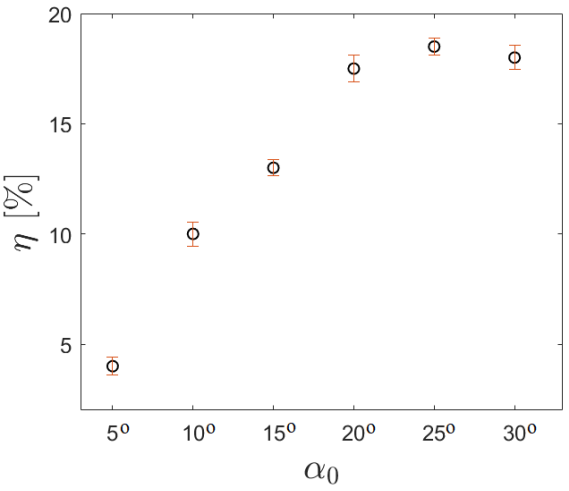

Figure 6.5: Efficiency coefficient versus α_0 and corresponding uncertainty bars for the quasi-2D flipper undergoing heave to pitch coupling.

combining these uncertainties so that:

$$\epsilon_\eta = \sqrt{(\frac{U_\infty}{P}\epsilon_T)^2 + (\frac{U_\infty F_x}{P^2}\epsilon_P)^2} \tag{6.3}$$

where F_x and P are the measured thrust and power respectively (see Chapter 2).

Since the St_A and $Re_\mathcal{C}$ are the same for all test cases, errors tend to vary only with the studied parameter namely, α_0 or AR. The maximum errors found by the above method, are rounded to one significant figure and are presented via error bars within the relevant figures of the following sections.

6.4 Results

6.4.1 Optimization of α_0

As mentioned above, quasi 2D experiments of the single foil are conducted so that the optimal α_0 is determined for the kinematic and flow parameters set earlier in this study (see section 6.1). More specifically we attempt to arrange the heave to pitch coupling in a way that minimizes energy dissipation. To this end, tests are performed for various α_0 from 5^o to 30^o at increments of 5^o.

Figure 6.5 shows the hydrodynamic efficiency of the flipper for various α_0. It can be observed that a large α_0 has a positive effect on the flipper´s performance but these benefits reach a plateau at about $\alpha_0 \sim 20^o - 25^o$. As the basis of this study is the work conducted by Muscutt et al. (2017a) where an $\alpha_0 \leq 20^o$ was used, it is decided that all later experiments will be conducted for $\alpha_0 = 20^o$.

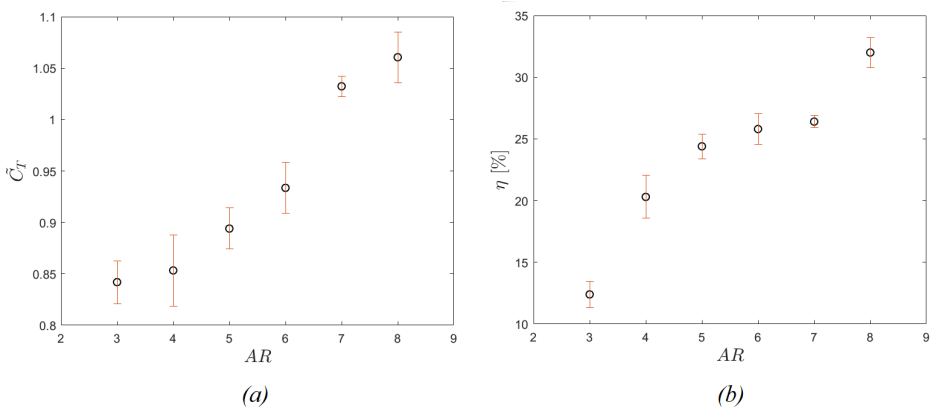

Figure 6.6: The impact of AR on the (a) thrust coefficient $\widetilde{C_T}$ and (b) efficiency with the corresponding uncertainty bars, for the single bio-inspired flipper.

6.4.2 AR effect on the single bio-inspired flipper

Having chosen the appropriate α_0 we proceed with our experiments on the bio-inspired single flappers of increasing AR. The impact of slenderness on the foil´s propulsion can be seen in figure 6.6. Following conventional wisdom, $\widetilde{C_T}$ seems to rise almost proportionally to AR (see figure 6.6a).Likewise, the hydrodynamic efficiency is increasing alongside the level of slenderness (see figure 6.6b), with the AR=8 reaching magnitudes observed for quasi-2D foils (Muscutt et al., 2017b). This behaviour is well documented in literature (Chopra, 1974; Chopra and Kambe, 1977; Cheng and Murillo, 1984; Karpouzian et al., 1990; Dong et al., 2006; Buchholz and Smits, 2008; Green and Smits, 2008; Shao et al., 2010; Dewey et al., 2013) although high AR wings are mostly prevalent among birds rather than aquatic animals (Ellington, 1984; Azuma, 1992; Usherwood and Ellington, 2002). The resemblance between our configuration and avian organisms should be expected as the current study is inspired by flipper-based propulsors utilizing an *underwater flight* pattern (Muscutt et al., 2017a; Robinson and JA, 1975; Tarlo, 1957; Tarsitano and Riess, 1982) rather than a fish-like undulatory motion based on a caudal fin.

In a three dimensional flow, the LEV´s and TEV´s of the flapping body form cylindrical structures, often connected via the tip vortices. Slenderness can benefit propulsion by weakening these tip vortices and/or by increasing the strength of the LEV´s. Here, $\tilde{\mathcal{C}} = 0.05\ m$ for all flippers. Thus, an increasing AR stretches the LEV´s on the spanwise direction, while keeping the available chordwise area constant for the tip structures. The resultant vortex bands appear elongated and come closer to the centerline where they blend with each other (see figure 6.7). This can benefit both the thrust and efficiency of the flipper by improving the cohesion and strength of the downstream jet, as momentum is redirected towards the U_∞.

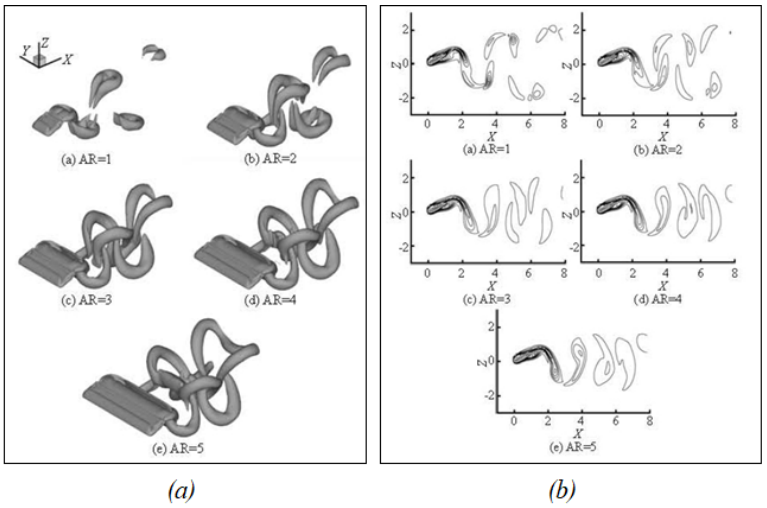

Figure 6.7: (a) Visualisation of differences in the wake development among flapping wings of increasing AR´s at $Re_{\mathcal{C}=}$. (b) Instantaneous vorticity field for the central cross section of the same flippers (where $Y = 0$ in the reference frame). Redrawn from Shao et al. (2010)

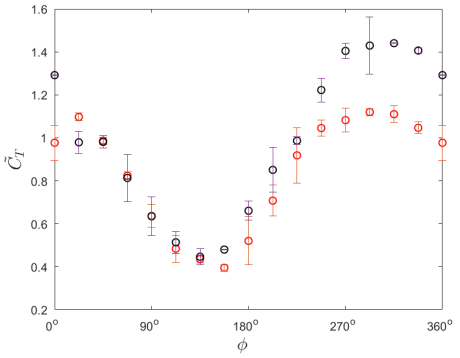

Figure 6.8: The impact of AR on the thrust coefficient $\widetilde{C_T}$ of the back foil with respect to ϕ for AR=3 (red) and AR=8 (black) with the corresponding uncertainty bars.

6.4.3 AR effect on the tandem bio-inspired configuration

The addition of another flipper in the upstream direction alters the flow field and determines the propulsive characteristics of the hint foil, as we see in figure 6.8 for the two extremes of the analysed AR range. Interestingly, the $\widetilde{C_T}$ of both cases varies in a sinusoidal fashion with respect to ϕ, showing a minimum at about $\phi \sim [112.5^o - 157.5^o]$ and a maximum at $\phi \sim [292.5^o - 315^o]$. This sinusoidal behaviour has been reported in numerous studies and is linked to the convection velocity of the TE vortices (Muscutt et al., 2017b,a). As mentioned before, thrust augmentation is achieved when the back foil weaves within the incoming vortices of the upstream wake. For a given spacing, this can only occur at a certain $\phi \leq 360^o$. Furthermore, there is also a single ϕ where $\widetilde{C_T}$ reaches its minimum as this coincides with the case where the back foil collides with the center of the incoming vortex. Therefore, the representation of the data via curve

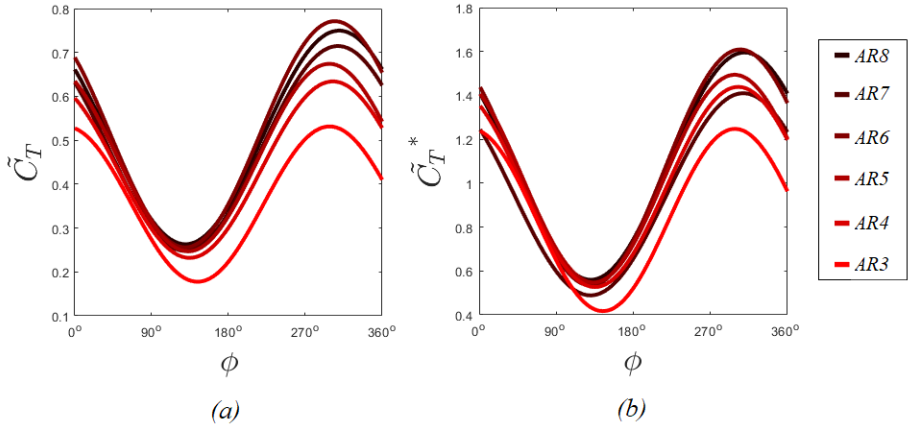

Figure 6.9: Best fit curves of the impact of AR on the back foil´s (a) thrust coefficient $\widetilde{C_T}$ and (b) relative thrust modification $\widetilde{C_T}^*$ with respect to ϕ. AR= 6 presents the highest optimum in both charts at a $\phi \sim 315°$.

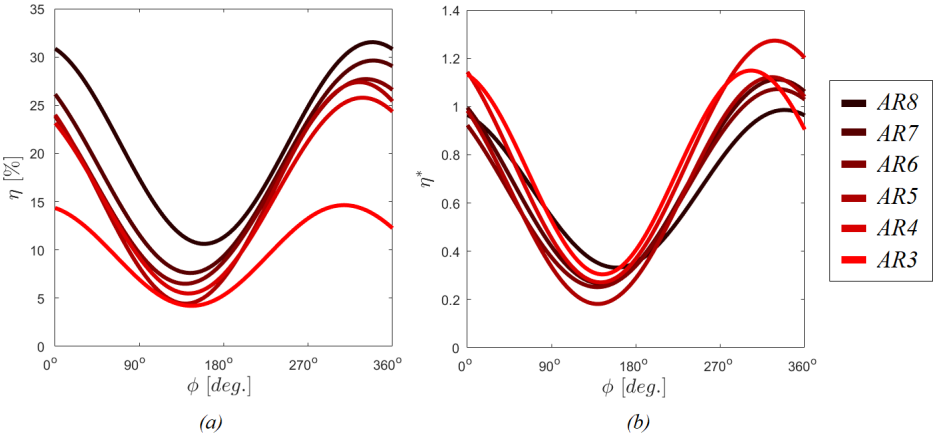

Figure 6.10: Best fit curves of the impact of AR on the back foil´s (a) efficiency and (b) relative efficiency versus ϕ for varying AR. Note that the optimum of most test cases is still located at $\phi \sim 315°$.

fittings of a first order Fourier model is deemed sufficient to preserve the main trend of the tandem system.

Figure 6.9 shows the best fitting curves of $\widetilde{C_T}$ and $\widetilde{C_T}^* = (\widetilde{C}_{T,b} - \widetilde{C}_{T,s})/\widetilde{C}_{T,b}$ for the tandem configuration at the full range of AR. Clearly, the back foil of all test cases experiences a peak in $\widetilde{C_T}$ augmentation within a range of $\phi \sim [270^o - 360^o]$ which agrees with the findings of similar research at the same St_A (Muscutt et al., 2017b,a). High AR´s seem to be more sensitive to ϕ as a greater $\Delta\widetilde{C_T}$ is observed between the best and the worst phase lag of these test cases in comparison with $AR \leq 5$. Furthermore, it is observed that an increasing AR leads to higher augmentation for the aft flipper of most test cases, possibly due to the more cohesive structure of the incoming wake as shown previously.

In terms of efficiency, tandem configurations seem to follow the trend of the single foil

where increasing the AR minimises the hydrodynamic loses (see figure 6.10 a). This consistency seems to be again the result of a more compact incoming wake, combined with the elongated LEV´s of the equally slender back flipper. It should be noted however that high AR´s take less advantage of the tandem configuration's wake recapture as they are already performing at an optimal level, allowing little room for improvement (see figure 6.10 b).

6.4.4 Comparison

Both single and tandem arrangements show improved thrust and efficiency coefficients when more elongated flippers are used. As a further step we investigate weather this sensitivity towards AR differs between the two configurations. To this end we present the propulsive performance of the single and the optimal hint foil for varying AR in figure 6.11.

Focusing on the thrust coefficient of the two foils (see figure 6.11a) we observe that apart from the augmentation experienced due to the wake recapture, the hint foil´s thrust curve differs also in shape. In particular, we notice that the sharp $\widetilde{C_T}$ increase at $AR \leq 5$ drops significantly at about $AR \sim 6$ and any further elongation has little to no effect. This is not the case for the single foil where $\widetilde{C_T}$ follows a steady increase even for the highest AR. This discrepancy can be attributed to vortex breaking on the spanwise direction. As the LEV´s grow stronger with slenderness they reach a limit after which any further momentum increase will affect their cohesion. In a tandem configuration, the LEV´s of the hint flipper are already enhanced by the energy harvested in the wake of the front. Therefore, it should be expected that their capacity to sustain the generated flow structures will be reduced.

In terms of hydrodynamic efficiency, no significant differences can be observed between the two configurations (see figure 6.11b). As mentioned previously, low AR´s benefit more from the dissipated energy in the wake of the front. However, as the single (front) flipper reaches an optimal level of performance at about $AR \sim 8$, little opportunity of increase is left for the hint. From a physics point of view this is again related to the wake pattern. In earlier sections we saw that low AR wings tend to generate small vortex rings that depart from the centerline in symmetric fashion. This results in high side forces at the cost of forward propulsion. A properly placed hint foil can redirect these structures towards the centerline and therefore benefiting efficiency. Yet, as the high AR´s tend to form relatively cohesive wakes which are tightly packed around the centerline, little further improvement can be expected from the interaction with an inline second flipper.

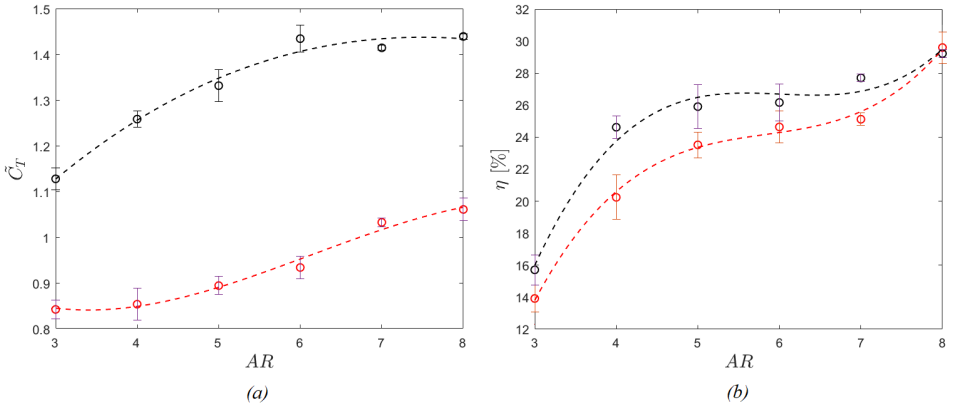

Figure 6.11: The impact of AR on (a) the thrust coefficient $\widetilde{C_T}$ and (b) the hydrodynamic efficiency η with the corresponding uncertainty bars, for the single (red) and the hint flipper of the tandem arrangement (black). Note that the points shown for the tandem configuration are the optimal values per ϕ. Best fit curves are represented with dashed lines.

6.5 Summary

The propulsive characteristics of single and tandem flapping foils were examined experimentally, for six flipper sets of $AR \sim [3-8]$ of a bioinspired geometry at $Re_{\mathcal{C}} = 8500$. Each set had the same AR and the test were conducted for the fixed combination $St_A = 0.4 - \mathcal{S}_C = 3$ and the full range of ϕ at increments of $\Delta\phi = 22.5^o$.

Our analysis shows that the thrust and efficiency coefficients increase with the AR in both configurations. This is a result of enhanced strength and cohesion on the foil´s wake which reduces the loses and allows for an optimal foil to foil interaction. Yet, thrust augmentation due to higher slenderness is limited by the spanwise breakdown of the LEV´s as a result of their increasing momentum. Since the back foil interacts with the incoming wake of the front, tandem configurations experience vortex breakdown at lower AR´s. This leads to the convergence of their thrust coefficients at AR = 6 while the single foil maintains a steady increase throughout the range of AR.

In terms of efficiency, low AR´s seem to benefit more from a tandem configuration as a badly conditioned front foil means more dissipated energy within the wake, which increases the potential of the back foil. On the other hand, no benefit was observed for the high AR´s efficiencies in tandem arrangement as the wake of the front foil is already oriented towards the centerline minimizing potential loses.

The evaluation of a flapping configuration based on the flipper geometry, can significantly reduce the effort of designing sufficient biomimetic propulsors. We believe that this study will enable the construction of more versatile bio inspired systems as it was demonstrated that performance parameters such as energy cost and maximum speed of the same mechanism can be modified according to the chosen flipper slenderness.

Chapter 7

Conclusions

Within this study we attempted to determine the propulsive characteristics of single and tandem flapping foils in the two and three dimensional domain. Our work involved computational analysis via a BDIM solver and load cell measurements on an underwater bio-ispired robotic setup. Our findings revealed crucial parameters of the single foil wake development, as well as the wake to wake interaction of a tandem foil configuration. In addition, we evaluated the effect of AR on the propulsive performance of single and identical tandem flipper arrangements.

With respect to the single foil, a reversed *von Kármán* street is responsible for the velocity surplus in the downstream wake, indicating the onset of thrust generation. However, the vortex pattern cannot be predicted based solely on the flapping peak-to-peak amplitude A and frequency f because the transition also depends sensitively on other details of the kinematics. We proposed an alternative method where A is replaced with the cycle-averaged swept trajectory $\mathcal{T}$ of the foil chord-line. Two dimensional simulations were performed for pure heave, pure pitch and a variety of heave-to-pitch coupling. In a phase space of dimensionless $\mathcal{T} - f$ we showed that the drag-to-thrust wake transition of all tested modes occurs for a modified Strouhal $St_{\mathcal{T}} \sim 1$. Physically the product $\mathcal{T}f$ expresses the induced velocity of the foil and indicates that propulsive jets occur when this velocity exceeds U_∞.

To further examine the validity of this metric we extended our analysis towards different foil thicknesses and the implementation of non-sinusoidal harmonic motions. The agreement was good for the new kinematics as they converged upon the same $St_{\mathcal{T}} \sim 1$ threshold. In a similar fashion, thickness to chord ratios within the range $D/\mathcal{C} = 12\% - 18\%$ experienced the *von Kármán* reversal at the aforementioned $St_{\mathcal{T}}$. On the other hand, significant discrepancies occurred outside this range suggesting that the metric cannot properly address very thin or very thick foils. As the definition of $\mathcal{T}$ is purely based on the kinematic input rather than the size and shape of the oscillating body, this issue was attributed to the limitations of the two dimensional solver. Yet, a verification of

this hypothesis required an extensive three dimensional analysis which was well beyond the scope of this study.

Our two dimensional analysis concluded with the tandem interaction of asymmetric wakes. Symmetric flapping foils are known to produce deflected jets at high frequency-amplitude combinations even at a zero mean angle of attack. This reduces the frequency range of useful propulsive configurations without side force. Here, we numerically analysed the interaction of these wakes for tandem flapping foils undergoing coupled heave to pitch motion. The impact of the flapping Strouhal number, foil spacing and phasing on wake interaction was investigated. Our primary finding was that the back foil is capable of cancelling the wake deflection and mean side force of the front foil, even when located up to 5 chord lengths downstream. This is achieved by attracting the incoming dipoles and disturbing their cohesion within the limits of the back foil's range of flapping motion. We also showed that the impact on cycle averaged thrust varies from high augmentation to drag generation depending on the wake patterns downstream of the back foil.

The experimental work of this project focused on the propulsive performance and 3D effects of single and tandem bio-inspired flapping arrangements undergoing heave to pitch coupling. Load cell measurements were conducted in a closed loop water tank, by utilizing a system of robotic probes. First we proceeded with the kinematic optimization by evaluating the hydrodynamic efficiency of quasi-2D rectangular flapping flippers for varying α_0 in a single foil arrangement. When the appropriate α_0 was chosen we continued with the investigation of the AR effect on single and tandem configurations of plesiosaur-inspired flippers for the same kinematics and flow conditions as in the quasi-2D study. Regarding the tandem arrangements, the flippers of each set had the same AR and were investigated for a fixed $\mathcal{S}_C$ and the full range of ϕ at increments of $\Delta\phi = 22.5^o$.

Our analysis showed that both thrust and efficiency benefit from high AR whether in single or tandem configurations but the phenomenon is limited by the spanwise breakdown of the LEV´s. Due to the wake recapture, this was more pronounced on the hint foil of the tandem arrangement and its $\widetilde{C_T}$ converged at AR = 6, while the single foil maintained a steady increase throughout the range of AR. In terms of efficiency, low AR´s seemed to profit more from a tandem arrangement as a badly conditioned front foil means more dissipated energy within the wake, which increases the potential of the back foil.

We believe that the findings of this study provide new insights towards the design of biomimetic tandem propulsors, as they expand their working envelope and enable a more accurate evaluation of the chosen geometry. In addition, they offer a unique insight into the thrust producing strategies of biological swimmers and flyers alike as they directly connect the wake development to the chosen kinematics enabling a self similar characterisation of flapping foil propulsion.

References

Akhtar, I., Mittal, R., Lauder, G. V., and Drucker, E. (2007). Hydrodynamics of a biologically inspired tandem flapping foil configuration. *Theoretical and Computational Fluid Dynamics*, 21(3):155–170.

Alexander, D. E. (1984). Unusual phase relationships between the forewings and hindwings in flying dragonflies. *Journal of Experimental Biology*, 109(1):379–383.

Andersen, A., Bohr, T., Schnipper, T., and Walther, J. (2017). Wake structure and thrust generation of a flapping foil in two-dimensional flow. *Journal of Fluid Mechanics*, 812.

Anderson, J., Streitlien, K., Barrett, D., and Triantafyllou, M. (1998). Oscillating foils of high propulsive efficiency. *Journal of Fluid Mechanics*, 360:41–72.

Ashraf, M., Young, J., and Lai, J. (2011). Reynolds number, thickness and camber effects on flapping airfoil propulsion. *Journal of Fluids and structures*, 27(2):145–160.

Azuma, A. (1992). Flight by beating. In *The Biokinetics of Flying and Swimming*, pages 77–154. Springer.

Azuma, A. (2006). *The Biokinetics of Flying and Swimming Second Edition*. AIAA Education Series.

Bakker, R. (1993). Plesiosaur extinction cycles—events that mark the beginning, middle and end of the cretaceous. *Evolution of the western interior basin. Geological Association of Canada, Special Paper*, 39:641–664.

Bandyopadhyay, P. R. and Leinhos, H. A. (2013). Propulsion efficiency of bodies appended with multiple flapping fins: When more is less. *Physics of Fluids*, 25:041902.

Betz, A. (1912). Ein beitrag zur erklaerung segelfluges. *Z Flugtech Motorluftschiffahrt*, 3:269–272.

Birnbaum, W. (1924). Das ebene problem des schlagenden flügels. *ZAMM-Journal of Applied Mathematics and Mechanics/Zeitschrift für Angewandte Mathematik und Mechanik*, 4(4):277–292.

Bohl, D. and Koochesfahani, M. (2009). MTV measurements of the vortical field in the wake of an airfoil oscillating at high reduced frequency. *Journal of Fluid Mechanics*, 620:63–88.

Boschitsch, B. M., Dewey, P. A., and Smits, A. J. (2014). Propulsive performance of unsteady tandem hydrofoils in an in-line configuration. *Physics of Fluids*, 26(5):051901.

Broering, T. M. and Lian, Y. (2012a). The effect of phase angle and wing spacing on tandem flapping wings. *Acta Mechanica Sinica*, 28:1557–1571.

Broering, T. M. and Lian, Y. (2012b). Numerical investigation of energy extraction in a tandem flapping wing con guration. *AIAA Journal*, 50:2295–2307.

Broering, T. M. and Lian, Y.-S. (2012c). The effect of phase angle and wing spacing on tandem flapping wings. *Acta Mechanica Sinica*, 28(6):1557–1571.

Buchholz, J. H. and Smits, A. J. (2006). On the evolution of the wake structure produced by a low-aspect-ratio pitching panel. *Journal of fluid mechanics*, 546:433–443.

Buchholz, J. H. and Smits, A. J. (2008). The wake structure and thrust performance of a rigid low-aspect-ratio pitching panel. *Journal of fluid mechanics*, 603:331–365.

Carlton, J. (1994). Marine propellers and propulsion. butterworth-heinemann great britain.

Chao, L.-M., Pan, G., Zhang, D., and Yan, G.-X. (2019a). Numerical investigations on the force generation and wake structures of a nonsinusoidal pitching foil. *Journal of Fluids and Structures*, 85:27–39.

Chao, L.-M., Pan, G., Zhang, D., and Yan, G.-X. (2019b). On the drag–thrust transition of a pitching foil. *Ocean Engineering*, 192:106564.

Cheng, H. and Murillo, L. E. (1984). Lunate-tail swimming propulsion as a problem of curved lifting line in unsteady flow. part 1. asymptotic theory. *Journal of Fluid Mechanics*, 143:327–350.

Chopra, M. (1974). Hydromechanics of lunate-tail swimming propulsion. *Journal of Fluid Mechanics*, 64(2):375–392.

Chopra, M. and Kambe, T. (1977). Hydromechanics of lunate-tail swimming propulsion. part 2. *Journal of Fluid Mechanics*, 79(1):49–69.

Cleaver, D., Wang, Z., and Gursul, I. (2012). Bifurcating flows of plunging aerofoils at high strouhal numbers. *Journal of Fluid Mechanics*, 708:349–376.

Couder, Y. and Basdevant, C. (1986). Experimental and numerical study of vortex couples in two-dimensional flows. *Journal of Fluid Mechanics*, 173:225–251.

Darwin, C. (2006). *On the Origin of Species by Means of Natural Selection or the preservation of the favoured races in the struggle for life.* The Folio Society, London.

de Kat, R. (2016a). *SESA6070-Lecture 10: Flow Visualization.* University of Southampton.

de Kat, R. (2016b). *SESA6070-Lecture 2: How well can we measure?* University of Southampton.

de Kat, R. (2016c). *SESA6070-Lecture 5: Forces.* University of Southampton.

Deng, J. and Caulfield, C. (2015). Three-dimensional transition after wake deflection behind a flapping foil. *Physical Review E*, 91(4):043017.

Dewey, P. A., Boschitsch, B. M., Moored, K. W., Stone, H. A., and Smits, A. J. (2013). Scaling laws for the thrust production of flexible pitching panels. *Journal of Fluid Mechanics*, 732:29.

Dong, H., Mittal, R., and Najjar, F. (2006). Wake topology and hydrodynamic performance of low-aspect-ratio flapping foils. *Journal of Fluid Mechanics*, 566:309.

Ellington, C. P. (1984). The aerodynamics of hovering insect flight. ii. morphological parameters. *Philosophical Transactions of the Royal Society of London. B, Biological Sciences*, 305(1122):17–40.

Fadlun, E., Verzicco, R., Orlandi, P., and Mohd-Yusof, J. (2000). Combined immersed-boundary finite-difference methods for three-dimensional complex flow simulations. *Journal of computational physics*, 161(1):35–60.

Fish, F. and Lauder, G. (2006). Passive and active flow control by swimming fishes and mammals. *Annu. Rev. Fluid Mech.*, 38:193–224.

Frey, E. and Riess, J. (1982). Considerations concerning plesiosaur locomotion. *Neues Jahrbuch für Geologie und Paläontologie, Abhandlungen*, 164:193–194.

Gibou, F., Fedkiw, R. P., Cheng, L.-T., and Kang, M. (2002). A second-order-accurate symmetric discretization of the poisson equation on irregular domains. *Journal of Computational Physics*, 176(1):205–227.

Godfrey, S. J. (1984). Plesiosaur subaqueous locomotion: a reappraisal. *Neues Jahrbuch für Geologie und Paläontologie, Monatshefte*, 11:661–672.

Godoy-Diana, R., Aider, J., and Wesfreid, J. (2008a). Transitions in the wake of a flapping foil. *Physical Review E*, 77(1):016308.

Godoy-Diana, R., Aider, J., and Wesfreid, J. (2008b). Transitions in the wake of a flapping foil. *Physical Review E*, 77(1):016308.

Godoy-Diana, R., Marais, C., Aider, J., and Wesfreid, J. (2009). A model for the symmetry breaking of the reverse bénard–von kármán vortex street produced by a flapping foil. *Journal of Fluid Mechanics*, 622:23–32.

Gong, W. Q., Jia, B. B., and Xi, G. (2015). Experimental study on mean thrust of two plunging wings in tandem. *AIAA Journal*, 53(6):1693–1705.

Gong, W. Q., Jia, B. B., and Xi, G. (2016). Experimental study on instantaneous thrust and lift of two plunging wings in tandem. *Experiments in Fluids*, 57(1):8.

Green, M. A. and Smits, A. J. (2008). Effects of three-dimensionality on thrust production by a pitching panel. *Journal of fluid mechanics*, 615:211–220.

Halstead, L. (1989). Plesiosaur locomotion. *Journal of the Geological Society*, 146(1):37–40.

He, G.-Y., Wang, Q., Zhang, X., and Zhang, S.-G. (2012). Numerical analysis on transitions and symmetry-breaking in the wake of a flapping foil. *Acta Mechanica Sinica*, 28(6):1551–1556.

Isogai, K., Shinmoto, Y., and Watanabe, Y. (1999). Effects of dynamic stall on propulsive efficiency and thrust of flapping airfoil. *AIAA journal*, 37(10):1145–1151.

Jaworski, J. W. and Gordnier, R. E. (2015). Thrust augmentation of flapping airfoils in low reynolds number flow using a flexible membrane. *Journal of Fluids and Structures*, 52:199–209.

Jones, K., Dohring, C., and Platzer, M. (1998). Experimental and computational investigation of the knoller-betz effect. *AIAA journal*, 36(7):1240–1246.

Jones, K., Lund, T., Platzer, M., et al. (2001). Experimental and computational investigation of flapping wing propulsion for micro air vehicles. *Progress in Astronautics and Aeronautics*, 195:307–339.

Karpouzian, G., Spedding, G., and Cheng, H. (1990). Lunate-tail swimming propulsion. part 2. performance analysis. *Journal of Fluid Mechanics*, 210:329–351.

Kato, N. (1998). Locomotion by mechanical pectoral fin. *Journal Marine Science and Technology*, 3:113–121.

Kinsey, T. and Dumas, G. (2012). Computational fluid dynamics analysis of a hydrokinetic turbine based on oscillating hydrofoils. *Journal of fluids engineering*, 134(2):021104.

Knoller, R. (1909). Die gesetzedes luftwiderstandes. *Flug-und Motortechnik (Wien)*, 3(21):1–7.

Koochesfahani, M. (1989). Vortical patterns in the wake of an oscillating airfoil. *AIAA journal*, 27(9):1200–1205.

Kozłowski, T. and Kudela, H. (2014). Transitions in the vortex wake behind the plunging profile. *Fluid Dynamics Research*, 46(6):061406.

Kruyt, J. W., Quicazán-Rubio, E. M., van Heijst, G. F., Altshuler, D. L., and Lentink, D. (2014). Hummingbird wing efficacy depends on aspect ratio and compares with helicopter rotors. *Journal of the royal society interface*, 11(99):20140585.

Kumar, A. and Hu, H. (2011). An experimental investigation on the wake flow characteristics of tandem flapping wings. In *6th AIAA theoretical fluid mechanics conference*, page 3120.

Lagopoulos, N. S., Weymouth, G. D., and Ganapathisubramani, B. (2019). Universal scaling law for drag-to-thrust wake transition in flapping foils. *Journal of Fluid Mechanics*, 872.

Lauder, G. V. (2015). Fish locomotion: recent advances and new directions. *Annual review of marine science*, 7:521–545.

Lehmann, F. O. (2009). Wing-wake interaction reduces power consumption in insect tandem wings. *Experiments in Fluids*, 46:765–775.

Lentink, D. and Dickinson, M. H. (2009). Rotational accelerations stabilize leading edge vortices on revolving fly wings. *Journal of Experimental Biology*, 212(16):2705–2719.

Lentink, D. and Gerritsma, M. (2003). Influence of airfoil shape on performance in insect flight. In *33rd AIAA Fluid Dynamics Conference and Exhibit*, page 3447.

Lewin, G. C. and Haj-Hariri, H. (2003). Modelling thrust generation of a two-dimensional heaving airfoil in a viscous flow. *Journal of Fluid Mechanics*, 492:339.

Lian, Y., Broering, T., Hord, K., and Prater, R. (2014). The characterization of tandem and corrugated wings. *Progress in Aerospace Sciences*, 65:41–69.

Licht, S., Polidoro, V., Flores, M., Hover, F. S., and Triantafyllou, M. S. (2004). Design and projected performance of a flapping foil auv. *IEEE Journal of oceanic engineering*, 29(3):786–794.

Lighthill, M. (1969). Hydromechanics of aquatic animal propulsion. *Annual review of fluid mechanics*, 1(1):413–446.

Long, J. H., Schumacher, J., Livingston, N., and Kemp, M. (2006). Four flippers or two? tetrapodal swimming with an aquatic robot. *Bioinspiration and Biomimetics*, 1(1):20.

Lu, K., Xie, Y., and Zhang, D. (2013). Numerical study of large amplitude, nonsinusoidal motion and camber effects on pitching airfoil propulsion. *Journal of Fluids and Structures*, 36:184–194.

Maertens, A. and Weymouth, G. (2015). Accurate cartesian-grid simulations of near-body flows at intermediate reynolds numbers. *Computer Methods in Applied Mechanics and Engineering*, 283:106 – 129.

Marais, C., Thiria, B., Wesfreid, J. E., and Godoy-Diana, R. (2012). Stabilizing effect of flexibility in the wake of a flapping foil. *Journal of Fluid Mechanics*, 710:659–669.

Mittal, R. and Balachandar, S. (1995). Effect of three-dimensionality on the lift and drag of nominally two-dimensional cylinders. *Physics of Fluids*, 7(8):1841–1865.

Mittal, R., Dong, H., Bozkurttas, M., Najjar, F., Vargas, A., and von Loebbecke, A. (2008). A versatile sharp interface immersed boundary method for incompressible flows with complex boundaries. *Journal of computational physics*, 227(10):4825–4852.

Muscutt, L. (2017). *The Hydrodynamics and Ecomorphology of Plesiosaurs*. PhD thesis, Faculty of Engineering and the Environment, University of Southampton.

Muscutt, L. E., Dyke, G., Weymouth, G. D., Naish, D., Palmer, C., and Ganapathisubramani, B. (2017a). The four-flipper swimming method of plesiosaurs enabled efficient and effective locomotion. *Proceedings of the Royal Society B: Biological Sciences*, 284(1861):20170951.

Muscutt, L. E., Weymouth, G. D., and Ganapathisubramani, B. (2017b). Performance augmentation mechanism of in-line tandem flapping foils. *Journal of Fluid Mechanics*, 827:484–505.

Newman, B. and Tarlo, L. H. (1967). A giant marine reptile from bedfordshire. *Animals*, 10(2):61–63.

Nudds, R. L., Taylor, G. K., and Thomas, A. L. R. (2004). Tuning of strouhal number for high propulsive efficiency accurately predicts how wingbeat frequency and stroke amplitude relate and scale with size and flight speed in birds. *Proceedings of the Royal Society, London*, 271:2071–2076.

O'Keefe, F. R. (2001). Ecomorphology of plesiosaur flipper geometry. *Journal of Evolutionary Biology*, 14(6):987–991.

Ol, M. V., Bernal, L., Kang, C. K., and Shyy, W. (2009). Shallow and deep dynamic stall for flapping low reynolds number airfoils. *Experiments in Fluids*, 46(5):883–901.

O'Keefe, F. R., Street, H. P., Wilhelm, B. C., Richards, C. D., and Zhu, H. (2011). A new skeleton of the cryptoclidid plesiosaur tatenectes laramiensis reveals a novel body shape among plesiosaurs. *Journal of Vertebrate Paleontology*, 31(2):330–339.

Park, H. and Choi, H. (2012). Kinematic control of aerodynamic forces on an inclined flapping wing with asymmetric strokes. *Bioinspiration and Biomimetics*, 7:15pp.

Peskin, C. S. (2002). The immersed boundary method. *Acta numerica*, 11:479–517.

Platzer, M. and Jones, K. (2008). Flapping wing aerodynamics-progress and challenges. In *44th AIAA Aerospace Sciences Meeting and Exhibit*, page 500.

Polet, D., Rival, D., and Weymouth, G. (2015). Unsteady dynamics of rapid perching manoeuvres. *Journal of Fluid Mechanics*, 767:323–341.

Politis, G. and Politis, K. (2014). Biomimetic propulsion under random heaving conditions, using active pitch control. *Journal of Fluids and Structures*, 47:139–149.

Raj, A. and Thakur, A. (2016). Fish-inspired robots: design, sensing, actuation, and autonomy—a review of research. *Bioinspiration & biomimetics*, 11(3):031001.

Ramamurti, R. and Sandberg, W. (2001). Computational study of 3D flapping foil flows. In *39th Aerospace Sciences Meeting and Exhibit*, page 605.

Read, D., Hover, F., and Triantafyllou, M. (2003). Forces on oscillating foils for propulsion and manoeuvering. *Journal of Fluids and Structures*, 17(1):163–183.

Rival, D., Hass, G., and Tropea, C. (2011). Recovery of energy from leading-and trailing-edge vortices in tandem-airfoil configurations. *Journal of Aircraft*, 48(1):203–211.

Robinson, J. A. (1977). Intracorporal force transmission in plesiosaurs. *Neues Jahrbuch fuer Geologie und Palaeontologie.*

Robinson, J. A. and JA, R. (1975). The locomotion of plesiosaurs.

Rohr, J. J. and Fish, F. E. (2004). Strouhal numbers and optimization of swimming by odontocete cetaceans. *The Journal of Experimental Biology*, 207:1633–1642.

Saharon, D. and Luttges, M. (1987). Three-dimensional flow produced by a pitching-plunging model dragonfly wing. In *25th AIAA aerospace sciences meeting*, page 121.

Salazar, R., Campos, A., Fuentes, V., and Abdelkefi, A. (2019). A review on the modeling, materials, and actuators of aquatic unmanned vehicles. *Ocean Engineering*, 172:257 – 285.

Schnipper, T., Tophøj, L., Andersen, A., and Bohr, T. (2010). Japanese fan flow. *Physics of Fluids (1994-present)*, 22(9):091102.

Shao, X.-m., Pan, D.-y., Deng, J., and Yu, Z.-s. (2010). Numerical studies on the propulsion and wake structures of finite-span flapping wings with different aspect ratios. *Journal of Hydrodynamics*, 22(2):147–154.

Spedding, G. R. (1987). The wake of a kestrel (falco tinnunculus) in flapping flight. *Journal of Experimental Biology*, 127:59–78.

Spiker, M., Thomas, J., Hall, K., Kielb, R., and Dowell, E. (2006). Modeling cylinder flow vortex shedding with enforced motion using a harmonic balance approach. In *47th AIAA/ASME/ASCE/AHS/ASC Structures, Structural Dynamics, and Materials Conference 14th AIAA/ASME/AHS Adaptive Structures Conference 7th*, page 1965.

Streitlien, K. and Triantafyllou, G. (1998). On thrust estimates for flapping foils. *Journal of fluids and structures*, 12(1):47–55.

Tarlo, L. (1957). The scapula of pliosaurus macromerus phillips. *Palaeontology*, 1(3):193–199.

Tarsitano, S. and Riess, J. (1982). Plesiosaur locomotion-underwater flight versus rowing. *Neues Jahrbuch für Geologie und Paläeontologie, Abhandlungen*, 164(1-2):188–192.

Taylor, G., Nudds, R., and Thomas, A. (2003). Flying and swimming animals cruise at a Strouhal number tuned for high power efficiency. *Nature*, 425(6959):707.

technical advisors, N. (2014). *LABVIEW: Users Manual*. National Instruments.

Thaweewat, N., Phoemsapthawee, S., and Juntasaro, V. (2018). Semi-active flapping foil for marine propulsion. *Ocean Engineering*, 147:556–564.

Thiria, B., Goujon-Durand, S., and Wesfreid, J. (2006). The wake of a cylinder performing rotary oscillations. *Journal of Fluid Mechanics*, 560:123–147.

Thomas, A. L. R., Taylor, G. K., Srygley, R. B., Nudds, R. L., and Bomphrey, R. J. (2004). Dragonfly flight: free-flight and tethered flow visualizations reveal a diverse array of unsteady lift-generating mechanisms, controlled primarily via angle of attack. *Journal of Experimental Biology*, 207(24):4299–4323.

Triantafyllou, G., Triantafyllou, M., and Grosenbaugh, M. (1993). Optimal thrust development in oscillating foils with application to fish propulsion. *Journal of Fluids and Structures*, 7(2):205–224.

Triantafyllou, G. S., Triantafyllou, M. S., and Chryssostomidis, C. (1986). On the formation of vortex streets behind stationary cylinders. *Journal of Fluid Mechanics*, 170:461–477.

Triantafyllou, M., Techet, A., and Hover, F. (2004). Review of experimental work in biomimetic foils. *IEEE Journal of Oceanic Engineering*, 29(3):585–594.

Triantafyllou, M., Triantafyllou, G., and Gopalkrishnan, R. (1991). Wake mechanics for thrust generation in oscillating foils. *Physics of Fluids A: Fluid Dynamics*, 3(12):2835—-2837.

Triantafyllou, M., Triantafyllou, G., and Yue, D. (2000). Hydrodynamics of fishlike swimming. *Annual Review of Fluid Mechanics*, 32(1):33–53.

Uhlmann, M. (2005). An immersed boundary method with direct forcing for the simulation of particulate flows. *Journal of Computational Physics*, 209(2):448–476.

Usherwood, J. R. and Ellington, C. P. (2002). The aerodynamics of revolving wings ii. propeller force coefficients from mayfly to quail. *Journal of Experimental Biology*, 205(11):1565–1576.

Usherwood, J. R. and Lehmann, F. O. (2008a). Phasing of dragonfly wings can improve aerodynamic efficiency by removing swirl. *Journal of the Royal Society, Interface*, 5:1303–1307.

Usherwood, J. R. and Lehmann, F.-O. (2008b). Phasing of dragonfly wings can improve aerodynamic efficiency by removing swirl. *Journal of The Royal Society Interface*, 5(28):1303–1307.

Vial, M., Bellon, L., and Hernández, R. (2004). Mechanical forcing of the wake of a flat plate. *Experiments in Fluids*, 37(2):168–176.

Von Ellenrieder, K., Parker, K., and Soria, J. (2003). Flow structures behind a heaving and pitching finite-span wing. *Journal of Fluid Mechanics*, 490:129–138.

Von Ellenrieder, K., Parker, K., and Soria, J. (2008). Fluid mechanics of flapping wings. *Experimental Thermal and Fluid Science*, 32(8):1578–1589.

Von Karman, T. (1935). General aerodynamic theory-perfect fluids. *Aerodynamic theory*, 2:346–349.

Von Mises, R. (1959). *Theory of flight*. Courier Corporation.

Wang, Z. (2005). Dissecting insect flight. *Annual Review of Fluid Mechanics*, 37(1):183–210.

Warkentin, J. and DeLaurier, J. (2007). Experimental aerodynamic study of tandem flapping membrane wings. *Journal of Aircraft*, 44(5):1653–1661.

Weymouth, G. (2014). Chaotic rotation of a towed elliptical cylinder. *Journal of Fluid Mechanics*, 743:385–398.

Weymouth, G., Devereux, K., Copsey, N., Muscutt, L., Downes, J., and Ganapathisubramani, B. (2017). Hydrodynamics of an under-actuated plesiosaur-inspired robot. *APS*, pages F9–003.

Weymouth, G. and Triantafyllou, M. (2012). Global vorticity shedding for a shrinking cylinder. *Journal of Fluid Mechanics*, 702:470.

Weymouth, G. and Yue, D. (2011). Boundary data immersion method for cartesian-grid simulations of fluid-body interaction problems. *Journal of Computational Physics*, 230(16):6233 – 6247.

Weymouth, G. D. (2016). Biologically inspired force enhancement for maritime propulsion and maneuvering. *arXiv preprint arXiv:1609.06559*.

Wiens, A. and Hosoi, A. (2018). Self-similar kinematics among efficient slender swimmers. *Journal of Fluid Mechanics*, 840:106–130.

Williamson, C. and Roshko, A. (1988). Vortex formation in the wake of an oscillating cylinder. *Journal of Fluids and Structures*, 2(4):355 – 381.

Xiao, Q. and Zhu, Q. (2014). A review on flow energy harvesters based on flapping foils. *Journal of Fluids and Structures*, 46:174–191.

Yan, J., Augier, B., Korobenko, A., Czarnowski, J., Ketterman, G., and Bazilevs, Y. (2016). Fsi modeling of a propulsion system based on compliant hydrofoils in a tandem configuration. *Computers and Fluids*, 141:201–211.

Zheng, Z. C. and Wei, Z. (2012). Study of mechanisms and factors that influence the formation of vortical wake of a heaving airfoil. *Physics of Fluids*, 24(10):103601.

Zurman-Nasution, A., Ganapathisubramani, B., and Weymouth, G. (2020). Influence of three-dimensionality on propulsive flapping. *Journal of Fluid Mechanics*, 886.